

Analysis of Orographic Precipitation and Isotopes in the Vicinity of the Patagonian Andes (latitude 54.8 to 40.1 S)

Mark T. Brandon¹, Queenie Chang², and Michael T. Hren²

Corresponding author: Mark Brandon mark.brandon@yale.edu

¹ Department of Earth and Planetary Sciences, Yale University, New Haven CT 06520, email: mark.brandon@yale.edu

² Department of Geosciences, University of Connecticut, Storrs, CT 06269

Citation

Brandon, M.T., Chang, Q., and Hren, M.T. (2022). Analysis of orographic precipitation and isotopes in the vicinity of the Patagonian Andes (latitude 54.8 to 40.1 S) (OPI-Patagonia_v1.001) [Data set]. Zenodo. <https://doi.org/10.5281/zenodo.7082538>, https://github.com/foret37/OPI-Patagonian-Andes/tree/OPI-Patagonia_v1.001

Overview

This report provides a compilation and analysis of precipitation isotope samples collected in the vicinity of the Patagonian Andes. These results are used as supplemental information for Brandon and Hren (2022) and Chang et al. (2022). Our overall objective is to establish a better understanding of the relationship between topography and precipitation isotopes, especially as applied to the study of the evolution of mountain ranges over geologic time.

The samples in our compilation were selected to be representative of the long-term (>1 year) average isotopic composition of precipitation at each location. Most samples were collected from rivers during base flow (summer months), when the water is primarily sourced by ground water. Ground water represents a mix of many precipitation events. This averaging is important because the geologic samples used in paleotopography studies also represent long-term averages of precipitation isotopes. We used the orographic precipitation and isotopes (OPI) programs of Brandon (2022) to find a best-fit solution for the precipitation climatology. Brandon et al. (2022) reports preliminary results on a similar study of orographic precipitation and precipitation isotopes in the South-Central Andes.

Water produced by precipitation is often called *meteoric water*, indicating that it fell from the sky. Thus, precipitation, precipitation water, and meteoric water are used here as synonyms.

There are three sections below. The first provides background information about precipitation and isotope fractionation associated with the flow of moist air over topography, and the relevance of this topic to the study of paleotopography. The second describes our compilation of precipitation isotopes. The third summarizes the analysis of the isotope data using the OPI programs.

Orographic Lifting, and Associated Precipitation and Isotope Fractionation

The “altitude effect” (Dansgaard, 1964) describes the common observation that the stable isotope composition of hydrogen and oxygen in precipitation tends to have a strong linear correlation with elevation of the sample. Ambach et al. (1968) provide an early example of this relationship, as demonstrated by isotope measurements of precipitation and glacial ice samples collected from elevation transects along modern glaciers in the Alps.

This empirical linear relationship has been widely used for almost three decades now to study the topographic evolution of mountain ranges over geologic time (e.g., Drummond et al., 1993; Norris et al., 1999; Garzione et al., 2000; Poage and Chamberlain, 2001; Rowley et al., 2001; Blisniuk and Stern, 2005; Rowley and Garzone, 2007). Norris et al. (1999) coined the term *isotope paleoaltimetry*. We prefer the term *isotope paleotopography*, because the isotopic fractionation occurs as moist air moves across the topography, and thus the amount of fractionation is only loosely linked to the elevation where the precipitation reaches the Earth’s surface.

Atmospheric science provides support for these ideas in that as moist air is forced to rise over mountainous topography, and the lifting causes an “orographic enhancement” in the precipitation rate (e.g., Smith and Barstad, 2004; Smith and Evans, 2007). Stable-isotope data provide a measure of this lifting given that the isotopic composition of water vapor in an air parcel and the precipitation that falls from that parcel become progressively lighter as the parcel moves downwind over progressively higher topography. The decrease in the $\delta^2\text{H}$ and $\delta^{18}\text{O}$ of precipitation is often considered to be linearly related to the elevation where the precipitation reached the ground, and this observation is often described by an *isotopic lapse rate*, which is defined by the decrease in $\delta^2\text{H}$ and $\delta^{18}\text{O}$ per kilometer of elevation. Poage and Chamberlain (2001) report a global compilation of stable isotopic data for meteoric water, and they suggest that the global-average isotopic lapse rate for $\delta^{18}\text{O}$ is 2.8 ‰/km. The 8:1 slope of the meteoric water line (Criss, 1999) indicates that the lapse rate for $\delta^2\text{H}$ should be about 22 ‰/km.

An implicit assumption of the isotope-paleotopography approach is that precipitation is created by stratified flow over the topography. Poulsen et al. (2010) argue that this assumption is not tenable in areas, such as the tropics, where a significant amount of precipitation is associated with convective instabilities. The mid-latitudes are affected by baroclinic instabilities (Holton and Hakim, 2013), which give rise to the migrating weather fronts and synoptic-scale precipitation events, which distinguish these regions. But note that both instabilities are initiated inside the atmosphere, and thus should be poorly correlated with the underlying topography.

This observation leads to the following interpretation. If convective and baroclinic instabilities are uncorrelated with topography, then the time-averaged precipitation rate associated with these instabilities should tend towards an approximately uniform value at the regional scale. In turn, precipitation formed by orographic lifting should be strongly correlated with the underlying topography, so the spatial distribution of time-averaged precipitation rates should be approximately fixed relative to the underlying topography. Furthermore, if the distribution of orographically-induced precipitation is stationary, then the spatial distribution of the precipitation isotopes should be stationary as well.

Another criticism of isotope-paleotopography comes from Galewsky (2008, 2009), who argues that the size of large mountain ranges results in partial blocking of the air flow over the topography, and this, in turn, reduces the amount of orographic lifting and the isotopic lapse rates as well. There is no doubt that topographic blocking is an important phenomenon. It was first recognized in the 1940s by glider pilots and by focused studies on mountain meteorology (see historical summaries in Smith, 2003, and Grubišić and Lewis, 2004). Thus, Galewsky's criticism is well founded. What is not yet resolved is if blocking has a significant influence on the long-term time-averaged spatial distribution of precipitation isotopes. Our analysis here provides diagnostics that we use to address this issue for our study. Given the importance of this question, we continue with a description of the blocking phenomenon.

Topographic blocking is often represented by a diagnostic variable, called the mountain-height number (Smith, 2003), which is defined by $M = N_m H_{\max} / U$, where U is the horizontal wind speed, H_{\max} is the maximum elevation in the study area, and N_m is the moist buoyancy frequency. The moist version of the buoyancy frequency, N_m (Durran and Klemp, 1982), is used here because precipitation requires saturated air. When M is small relative to one, the wind field tends to flow up and over the mountain topography. As M approaches one, the wind field will start to be deflected laterally around the mountain topography, which means that there is less lifting and less precipitation. As M exceeds about 1.2 to 1.5, the wind field transitions to a nonlinear regime, which is marked by unsteady vortices and eddies, and breaking waves above the leeside of the mountain.

M is defined at the scale of the full model domain. We find it more useful to use a local measure of blocking, defined by the horizontal wind speed ratio at a point. The concept is simple, but some background is needed before this ratio is defined. Let's consider a simplified definition of the problem, where an arbitrary mountain range lies within a much larger wind field. At the regional scale, the wind field is characterized by a uniform and steady horizontal wind velocity with a magnitude U . In the modeling discussed below, we call this the base-state wind field (see Brandon, 2022, for details). Next, we define a right-handed coordinate system with the x axis oriented in the downwind horizontal direction of the base-state wind field. The y axis is in the horizontal counterclockwise normal direction relative to the x axis, and the z axis is vertical and up. The wind vector at an x, y, z point is defined by velocity components u , v , and w , which are referenced to the x , y , and z axes, respectively.

As an example, the base-state wind field is uniform across the model domain, so the velocity components are uniform as well, with $u = U$, and $v = w = 0$. If we insert the mountain topography into this wind field, the wind-velocity field, as defined by $u(x, y, z)$, $v(x, y, z)$, $w(x, y, z)$, is perturbed to new values. The practice is to focus on the perturbed components of the wind field, which are given by $u' = u - U$, $v' = v$, and $w' = w$. (See Holton and Hakim, 2013, chap. 5 for a summary of the use of perturbation variables for modeling atmospheric flow.)

For analysis of topographic blocking, we focus on how u and u' vary relative to U . With this in mind, we define the horizontal velocity ratio as u'/U . If we use the term in a strict sense, then blocking would describe locations where $u'/U \leq -1$, which means that horizontal wind speed parallel to the base-state wind direction is stalled at zero ($u = 0$) or has a reverse sense of flow ($u < 0$) relative to the base-state.

Blocking is usually associated with slow or reversed low-level winds over the windward side of a mountain and fast low-level winds over the leeward side. Thus, as a diagnostic, we can be confident that block is insignificant if the horizontal velocity ratio lies in the range $-1 < u'/U < 1$.

In the analysis below, we construct a map that shows the distribution of u'/U at the land surface. The reason is that magnitude of this ratio decreases upward from a point on the land surface, so the view at the bottom of the atmosphere is sufficient to determine where blocking might be a problem.

Precipitation Isotope Data

The Patagonian Andes refer to the southern continuation of the Andes, starting at about 37° S latitude. The samples considered here span from 40.1° to 54.8° S latitude. The maximum elevation in this region is 4058 m (Cerro San Valentín, at 49.6° S).

We compiled 554 analyses of modern meteoric water in a 1635×530 km area covering the Patagonian Andes and adjacent lowlands. These data are made available here in an Excel spreadsheet, entitled “Patagonia Andes North and South Isotopes 29 Jun 2021.xlsx”.

Our group is responsible for 243 of these analyses: 9 were collected by David Colwyn in 2013, 53 by David Colwyn and Astrid Pacini in 2015, 97 by Queenie Chang in 2017 and 2018, 9 by Greg De Pascale in 2017. The analyses collected by Colwyn were published in Colwyn et al. (2019). Almost all of our samples were collected from rivers. All sampling was done during summer months to ensure base-flow conditions for the river samples. All samples were placed in sealed glass vials, to avoid evaporation.

The remaining 311 analyses in our compilation are from other published sources: 3 from Global Network for Isotopes in Precipitation (GNIP) stations (International Atomic Energy Association, 2019), 98 from Stern and Blisniuk (2002), 69 from Smith and Evans (2007), and 141 from Mayr et al. (2018). The samples for these analyses were also collected in summer months, using standard sampling procedures. For Mayr et al. (2018), we used their “lentic (upwind)”, “lotic (upwind)”, and “lotic (downwind)” analyses (lentic = slow-moving water, such as lakes, lotic = fast-moving water, such as rivers). In general, we prefer to avoid lake samples because of the greater potential for evaporation, but the upwind lake samples from Mayr et al. had isotopic values that indicated minimal post-precipitation evaporation. These were need to provide sufficient sampling density on the Chilean side of the study area. We did not use their “precipitation samples (upwind)”, “precipitation samples (downwind)”, and “lentic waters (downwind)” because the sampling interval was too short (precipitation samples) or because the lake samples from the Argentina side of the study showed evidence for significant post-precipitation evaporation.

Our compilation is focused on samples that are representative of the long-term time-averaged isotopic composition of the precipitation isotopes in the vicinity of the sample location. We distinguish between a *local sample*, where the sampled water is representative of the precipitation that fell at the sample location, and a *catchment sample*, where the sampled water

came from a river or lake and thus is a mixture of the precipitation that fell within the catchment upriver of the sample location.

All but three of our samples are catchment samples. Collection during the summer ensures that the waters are mainly due to discharge of ground water. Natural ground water originates from precipitation that falls within the upslope catchment above the sample location. The residence time of ground water that discharges in small catchments is estimated to be about 1 to 3 years (McGuire and others, 2005), which indicates that the water and its stable isotopes are averaged over many precipitation events.

The local samples come from three GNIP stations. The reported isotopic compositions for these samples are precipitation-weight averages for the sequence of reported monthly analyses for each GNIP station.

We use the terms *primary* and *altered* to indicate if the sample has seen significant post-precipitation evaporation, as indicated by the “deuterium excess” variable, where $d = \delta^2\text{H} - 8\delta^{18}\text{O}$ (Criss, 1999). Primary samples, with $d > 5$ per mil, are considered to have isotopic compositions that formed solely by condensation and precipitation, and altered samples, with $d < 5$ per mil, are considered to have been altered by subsequent evaporation. Chang et al. (2022) provides evidence that the 5 per mil threshold provides a reliable criterion for separation between primary and altered samples. We include both samples in the OPI analysis below. The programs make the distinction between primary and altered, and treats the samples accordingly.

Selection Criteria

The data set was reduced using the following criteria:

- 1) Samples that lacked paired measurements of $\delta^2\text{H}$ and $\delta^{18}\text{O}$ were rejected.
- 2) The original data generally include information about the elevation of each sample. We assessed the reliability of the reported locations by comparing the reported elevation, with an elevation calculated from a high-resolution digital elevation model using the reported longitude and latitude. A sample was rejected when there was a significant difference between these two elevations, and if it was not possible to correct the location.
- 3) Samples located outside of the study area were rejected (e.g., 1 GNIP sample and 2 river samples from Ushuaia, located at 54.8°S latitude).
- 4) Samples of glacial ice or direct runoff from a glacier, and samples that were collected near agricultural settings, ponds, or lakes were rejected. Exceptions were made for upwind samples of lake water from Mayer et al. (2018). Deuterium-excess values for these samples indicate that they are representative of primary precipitation.
- 5) Samples with isotopic compositions that are anomalously low or high relative to other nearby samples were rejected.

- 6) Samples from GNIP sites were rejected if the sampling interval was shorter than 20 months.
- 7) Replicate analyses were averaged to get a single value for each location. One might consider using these replicates to estimate errors and develop statistical weights for each sample location. We did not do this because we have found, from our least-squares estimates, that the uncertainties associated with the determination of the stable isotope concentrations are much smaller than the total error associate with each sample. The reason is that the total error is dominated by natural variation.

The reduced dataset used for our OPI analysis is composed of sample compositions from 449 unique locations. The following provides the breakdown of the samples by category:

Primary catchment samples: 304

Primary local sample (GNIP station): 1

Altered catchment samples: 143

Altered local sample (GNIP station): 1

Results of OPI Analysis

We used the OPI programs to analyze the stable isotope data. These programs provide a full representation of the steady flow of moist air over an arbitrary 3D topography, and the downwind evolution of water vapor, cloud water, precipitation, and the stable isotope composition for these water species. The catchment region is calculated for each catchment sample, and used to integrate the precipitation and precipitation isotopes captured by the catchment.

The OPI model expands on the “linear theory of orographic precipitation” (LTOP) model of Smith and Barstad (2004). Lin (2007) and Nappo (2013) provide comprehensive descriptions of analytic basis for the wind field, including the governing Euler equations, and the Fourier solution for steady flow of a buoyantly stratified atmosphere over a 3D topography.

OPI includes three major features that distinguish it from LTOP. The first is that the OPI uses the moist Euler equations from Durran and Klemp (1982), which means that N_m is uniform throughout the overlying atmosphere.

The second feature is that the OPI model calculates a full balance for all water species in the model, which is essential for precise estimation of the isotope evolution of these species. The LTOP model does not include a water balance. This decision appears to have been motivated by a desire to keep the model simple, and by the expectation that the loss due to precipitation would be small relative to the water vapor flux. Smith and Evans (2007, see their appendix) introduce an adjustment to the LTOP model to improve the water balance.

The third feature is that OPI includes a full path integration of the isotope fractionation of atmospheric water vapor, and cloud water moving along the wind path, and the associated precipitation that separates and falls to the base of the model, and water vapor generated by evaporation of that precipitation as it falls. The influence of the local temperature on fractionation and exchange is also included. These calculations are the same as those used in isotope-enabled global climate models (GCMs) and regional climate models (RCMs).

The current generation of GCMs and RGMs are often viewed as the optimal way to study atmospheric processes. Many models are “isotope enabled” in that they can account for the evolution of the isotopic composition of all species of water within the model domain (Boysun and Ehler, 2021). These numerical models provide a fully coupled calculation of atmospheric flow, radiative and heat transfer, cloud formation, and the formation and fallout of precipitation. Thus, why would one want to use a simpler model, such as OPI.

One reason is that GCMs and RCMs are computationally intensive, which requires a tradeoff, where the horizontal resolution is decreased to less than optimal values to get reasonable run times. As a result, GCMs current have a horizontal resolution of about 100 to 50 km, and RCMs, about 20 to 10 km, which means that topography is poorly represented in these models.

We use the LTOP model (Smith and Barstad, 2004) to guide our estimate of the grid resolution needed to represent orographic precipitation. The LTOP model shows that the relationship between topography and precipitation is best represented using Fourier components for the topography, and that all wavelengths of the topography can contribute significantly to the overall precipitation. Thus, the grid resolution required to represent orographic precipitation is not set by the process itself, but rather by the spectral distribution of natural topography. Fourier analysis shows that natural topography generally follows a Brownian distribution, where the amplitude of the Fourier components falls off proportionally with the square-root of the wavelength (Turcotte and Huang, 1995; Malamud and Turcotte, 1999). Using these scaling relationships, we have found that a grid spacing of about 1 km is required to represent the orographic process. The OPI algorithm can compute a full 3D solution for our entire study area at 1 km grid resolution in about 1 to 2 minutes using a current high-end personal computer.

An additional issue is that the current GCMs and RCMs generally do a poor job predicting precipitation and available observations for precipitation have problems as well (Ban et al., 2021; Marin et al., 2018; Tapiador et al., 2017, 2019; Wheeler et al., 2017). As an example, Ban et al. (2021) show, using high-resolution modeling with six different RGMs, that estimation of the precipitation field improves as the horizontal resolution is increased from a 12 to 15 km grid to a 2 to 3 km grid. The authors found an improvement in the models, but there were still differences between the models, and uncertainties about the observations.

Another issue is the GCMs and RCMs are designed to solve the time-evolution of the climate system. The isotope-paleotopography method is focused on using the time-averaged composition of precipitation isotopes to estimate the topography upwind of the sample site. Thus, the time-varying history of the precipitation field is of little use for our application. In addition, our paleotopography applications are focused on understanding the precipitation generated by orographic lifting. The LTOP and OPI models are based on steady-state solutions for the precipitation caused by orographic lifting, and thus they are well matched for understanding the time-averaged distribution of isotopes associated with orographic precipitation.

The OPI programs include the option to find a least-squares fit of the meteoric water isotope data relative to the model, and a best-fit estimate of a set of OPI parameters. The search for a best-fit

solution requires a minimum of about 15,000 solutions, so this option is only possible given the fast solution time for the OPI algorithm.

A “one-wind” solution is defined by nine parameters: mean wind speed U , mean wind direction *azimuth*, sea-level surface-air temperature T_0 , mountain-height number M , horizontal eddy diffusivity κ , mean residence time for cloud water τ_c , the hydrogen isotopic composition of base precipitation at the centroid of the sample data $\delta^2\text{H}_0$, the latitudinal gradient of hydrogen isotopic composition of base precipitation $d(\delta^2\text{H}) / d(\text{latitude})$, and the fraction of precipitation remaining after evaporation f_p .

The output from OPI programs is reported below. Brandon (2022) provides details about the design of the OPI programs, the definition of terminology and parameters, and the interpretation of results.

We follow here with a summary of the main conclusions, with an emphasis on those that are most relevant for the Brandon and Hren (2022) and Chang et al. (2022) papers.

- 1) We conducted more than 75 runs to test and confirm the best-fit OPI solution for the Patagonia Andes isotope data. These runs included calculating best-fit solutions for the south and north halves of the region, and using a two-wind model for the full region. A one-wind least-squares solution takes about 5 hours on a cluster with 27 CPUs running in parallel and sharing 75 GB of memory.
- 2) The runs clearly indicate that the isotope data are best-fit by a “one-wind” solution for the full region. The fit indicates the errors for the stable isotope data have reasonable standard deviations, equal to 10.4 per mil for $\delta^2\text{H}$ and 1.3 per mil for $\delta^{18}\text{O}$. The figures produced by `opiPlots_OneWind` provides a good demonstration of the fit of the data relative to the model. The estimated parameters seem physically plausible and reasonable. All estimated parameters are well resolved (see uncertainties in the log page for `opiPairPlots`).

Best-Fit Precipitation State

Wind speed (m/s): 11.8 m/s

Azimuth: 109.2 degrees

Sea-level temperature: 281.5 K (8.3 °C)

Mountain-height number: 0.187 (dimensionless)

Horizontal eddy diffusivity: 0 m²/s

Average residence time for cloud water: 140 s

$\delta^2\text{H}$ for base precipitation: -43.6 per mil

$\delta^2\text{H}$ latitude gradient for base precipitation: -0.859 per mil/deg lat (abs value of latitude)

Residual precipitation after evaporation: 0.82 (fraction)

- 3) The solution reported above includes an estimate for evaporative recycling. The issue here is not about the primary samples, which were screened to avoid post-precipitation evaporation. Rather, this estimate, called the “residual precipitation after evaporation”, indicates the fraction of precipitation formed within the model domain that leaves the bottom of the

model, as ground water. The estimate is 0.82, which means that 0.18 of the precipitation is lost by evaporation as it falls through the atmosphere. This recycling is thought to occur as precipitation falls through dry regions in the atmosphere. The efficiency of the precipitation process is reduced as the amount of evaporative recycling increases. Likewise, the amount of isotope fractionation is reduced as well. Chang et al. (2022) provides more on this topic of evaporative recycling in Patagonian Andes.

- 4) The OPI programs assume that all precipitation is due to stratiform flow of moist air over topography. The good fit of the model to the data suggests that this simplification is reasonable. But note that stratiform flow is expected given that our study area is in the subtropics.
- 5) The best-fit solution shows the mountain-height number, M , is 0.187. Figure 12 in *opiMaps_OneWind* shows the horizontal velocity ratio, u'/U at the land surface. The magnitude $|u'/U|$ is less than ~0.6. Likewise, the streamlines for the estimated wind field (figure 7 in *opiMaps_OneWind*) pass undeflected over the mountain range. This evidence clearly indicates that topographic blocking is not a factor for the orographic precipitation field over the Patagonian Andes. The moist buoyant frequency has an estimated value $N_m = 0.639$ mrad/s. Most authors envision a much larger average value for the buoyance frequency of the troposphere, equal to about 10 mrad/s (e.g., Holton and Hakim, 2013, p. 56). This result may resolve the debate of the influence of blocking on orographic precipitation in that the actual value for N_m is smaller than expected.
- 6) Figure 6 in *opiPlots_OneWind* shows a crude linear relationship between isotopic fractionation and local elevation, which is consistent with the concept of “isotope paleotopography”. Figure 5 shows that there is a very good fit when local elevation is replaced by *maximum lifting*, which is defined as the maximum elevation along the path upwind of the sample point.
- 7) The best-fit OPI solution indicates an $\delta^2\text{H}$ isotopic lapse rate of 29 per mil/km (see log file for *opiPlots_OneWind*). This result is greater than the global estimate by Poage and Chamberlain (2001), which indicates a $\delta^2\text{H}$ lapse rate of 22 per mil/km.

Acknowledgements

We thank Greg De Pascale and Rebecca VanderLeest for help with sampling in the field. Our research was supported, in part, by US National Science Foundation grants, NSF EAR-1650313 and EAR-1650396 to Mark Brandon and Michael Hren, respectively.

References

Ambach, W., W. Dansgaard, H. Eisner & J. Møller (1968) The altitude effect on the isotopic composition of precipitation and glacier ice in the Alps, *Tellus*, 20:4, 595-600, DOI: 10.3402/tellusa.v20i4.10040

Ban, N., Caillaud, C., Coppola, E., Pichelli, E., Sobolowski, S., Adinolfi, M., Ahrens, B., Alias, A., Anders, I., Bastin, S. and Belušić, D., 2021. The first multi-model ensemble of regional

climate simulations at kilometer-scale resolution, part I: evaluation of precipitation. Climate Dynamics, 57(1), pp.275-302.

Blisniuk, P., and Stern, L., 2005, Stable isotope paleoaltimetry: A critical review: American Journal of Science, v. 305, p. 1033.

Brandon, M.T. (2022). MATLAB programs for the analysis of orographic precipitation and isotopes, with implications for the study of paleotopography (OPI 3.6). Zenodo.

<https://doi.org/10.5281/zenodo.7063327>, <https://github.com/foret37/OPI-Orographic-Precipitation-and-Isotopes/tree/v3.6.002>

Brandon. M.T., and Hren, M.T., 2022, A process-based analysis of precipitation isotopes and topography in the Patagonian Andes, with implications for the study of paleotopography. In preparation.

Brandon, M.T., Fennell, L.M., Hren, M.T. (2022). Analysis of orographic precipitation and isotopes in the vicinity of the South-Central Andes (latitude 37.6 to 32.4 S) (OPI-SCA 1.0.000). Zenodo. <https://doi.org/10.5281/zenodo.7077390>, https://github.com/foret37/OPI-South-Central-Andes/tree/OPI-SCA_v1.0.001

Botsyun, S. and Ehlers, T.A., 2021. How can climate models be used in paleoelevation reconstructions? Frontiers in Earth Science, v. 9, p. 624542.

Chang, Q., Brandon, M.T., and Hren, M.T., 2022, Topography, evaporation and precipitation isotopes across the Patagonian Andes (in review).

Colwyn, D. A., Brandon, M. T., Hren, M. T., Hourigan, J., Pacini, A., Cosgrove, M. G., Midzik, M., Garreaud, R. D., and Metzger, C., 2019, Growth and steady state of the Patagonian Andes: American Journal of Science, v. 319, p. 431–472.

Criss, R.E., 1999. Principles of stable isotope distribution. Oxford University.

Dansgaard, W., 1964, Stable isotopes in precipitation: Tellus, v. 16, p. 436–468.

Drummond, C. N., Wilkinson, B. H., Lohmann, K. C., and Smith, G. R., 1993, Effect of regional topography and hydrology on the lacustrine isotopic record of Miocene paleoclimate in the Rocky Mountains: Palaeogeography, Palaeoclimatology, Palaeoecology, v. 101, p. 67–79.

Durran, D., and Klemp, J., 1982, On the effects of moisture on the Brunt–Vaisala frequency: Journal of the Atmospheric Sciences, v. 39, p. 2152–2158.

Galewsky, J., 2008. Orographic clouds in terrain-blocked flows: An idealized modeling study. Journal of the Atmospheric Sciences, 65(11), p.3460-3478.

Galewsky, J., 2009. Rain shadow development during the growth of mountain ranges: An atmospheric dynamics perspective. Journal of Geophysical Research: Earth Surface, 114 (F1).

Garzione, C. N., Dettman, D. L., Quade, J., DeCelles, P. G., and Butler, R. F., 2000, High times on the Tibetan Plateau: Paleoelevation of the Thakkola graben, Nepal: *Geology*, v. 28, p. 339–342.

Holton, J. R., and Hakim, G. J., 2013, An introduction to dynamic meteorology: Academic Press, Academic Press.

International Atomic Energy Association, 2019, Global network of isotopes in precipitation (GNIP). http://www-naweb.iaea.org/napc/ih/IHS_resources_gnip.html

Lin, Y.L., 2007. Mesoscale dynamics (Vol. 630). Cambridge: Cambridge University Press.

McGuire, K. J., McDonnell, J. J., Weiler, M., Kendall, C., McGlynn, B. L., Welker, J. M., and Seibert, J., 2005, The role of topography on catchment-scale water residence time: *Water Resources Research*, v. 41, no. 5, DOI:10.1029/2004WR003657.

Malamud, B.D. and Turcotte, D.L., 1999. Self-affine time series: I. Generation and analyses. In *Advances in Geophysics* (Vol. 40, pp. 1-90). Elsevier.

Martin, A., Ralph, F.M., Demirdjian, R., DeHaan, L., Weihs, R., Helly, J., Reynolds, D. and Iacobellis, S., 2018. Evaluation of atmospheric river predictions by the WRF Model using aircraft and regional mesonet observations of orographic precipitation and its forcing. *Journal of Hydrometeorology*, 19(7), pp.1097-1113.

Mayr, C., Langhamer, L., Wissel, H., Meier, W., Sauter, T., Laprida, C., and Lücke, A., 2018, Atmospheric controls on hydrogen and oxygen isotope composition of meteoric and surface waters in Patagonia. *Hydrology and Earth System Sciences Discussions*, 1-22.

Nappo, C.J., 2013. An introduction to atmospheric gravity waves. Academic Press.

Norris, R. D., Corfield, R. M., and Hayes-Baker, K., 1999, Mountains and Eocene climate, in, p. 161–196.

Poage, M., and Chamberlain, C., 2001, Empirical relationships between elevation and the stable isotope composition of precipitation and surface waters: Considerations for studies of paleoelevation change: *American Journal of Science*, v. 301, p. 1–15.

Poulsen, C. J., Ehlers, T. A., and Insel, N., 2010, Onset of Convective Rainfall During Gradual Late Miocene Rise of the Central Andes: *Science*, v. 328, p. 490.

Rowley, D., Pierrehumbert, R., and Currie, B., 2001, A new approach to stable isotope-based paleoaltimetry: implications for paleoaltimetry and paleohypsometry of the High Himalaya since the Late Miocene: *Earth and Planetary Science Letters*, v. 188, p. 253–268.

Rowley, D. B., and Garzione, C. N., 2007, Stable isotope-based paleoaltimetry: Annual Review of Earth and Planetary Sciences, v. 35, p. 463–508.

Smith, R. B., 2003, Stratified flow over topography, in Environmental stratified flows: Springer, Boston, MA, p. 119–159.

Smith, R. B., and Barstad, I., 2004, A Linear Theory of Orographic Precipitation: Journal of the Atmospheric Sciences, v. 61, p. 1377–1391.

Smith, R. B., and Evans, J., 2007, Orographic precipitation and water vapor fractionation over the southern Andes: Journal of Hydrometeorology, v. 8, p. 3–19.

Stern, L. A., and Blisniuk, P. M., 2002, Stable isotope composition of precipitation across the southern Patagonian Andes. Journal of Geophysical Research: Atmospheres, 107(D23), ACL-3

Tapiador, F.J., Navarro, A., Levizzani, V., García-Ortega, E., Huffman, G.J., Kidd, C., Kucera, P.A., Kummerow, C.D., Masunaga, H., Petersen, W.A. and Roca, R., 2017. Global precipitation measurements for validating climate models. Atmospheric Research, 197, pp.1-20.

Tapiador, F.J., Roca, R., Del Genio, A., Dewitte, B., Petersen, W. and Zhang, F., 2019. Is precipitation a good metric for model performance? Bulletin of the American Meteorological Society, 100(2), pp.223-233.

Turcotte, D.L. and Huang, J., 1995. Fractal distributions in geology, scale invariance, and deterministic chaos. In Fractals in the earth sciences (pp. 1-40). Springer, Boston, MA.

Wheeler, M.C., Zhu, H., Sobel, A.H., Hudson, D. and Vitart, F., 2017. Seamless precipitation prediction skill comparison between two global models. Quarterly Journal of the Royal Meteorological Society, 143(702), pp.374-383.

opiFit_OneWind

Program: opiFit_OneWind
Start time: 18-Aug-2021 21:25:00

Run file path:

/Users/markbrandon/Dropbox (Yale University)/OPI Patagonia/Runs_NP-SP/run024_NP-SP

Leeside evap, nEvap = 1, more samples BEST SOLUTION

Run filename:

run024_NP-SP TEST.run

Run title:

run 024, north & south Patagonia, opi 3.6 with lee-side evaporation, free kappa, and new samples

Path name for data directory:

~/Dropbox/OPI Patagonia/data Patagonia

----- Topography File -----

Topography file: Patagonia topography_Gebco1km.mat

Maximum elevation: 3457 m

Grid size, nx and ny: 1365, 2114

Minimum and maximum for longitude: -80, -62.5 degrees

Minimum and maximum for latitude: -55, -36 degrees

Grid spacing, dx and dy: 0.0128299, 0.00899195 degrees

Grid spacing, dx and dy: 0.98, 1.00 km

Lon, lat for map origin: -72.661, -46.765 degrees

Map origin is set to sample centroid.

Size of cosine window as fraction of grid size: 0.250000 (dimensionless)

Coriolis frequency at map-origin latitude: -0.106253 mrad/s

Lon, lat for section origin: -72.661, -46.765 degrees

----- Sample File -----

Sample file: Patagonia Andes North and South Isotopes 29 Jun 2021.xlsx

Number of all samples: 449

Number of altered samples: 144

Number of primary samples: 305

Number of local primary samples: 1

Number of catchment primary samples: 304

Minimum and maximum for longitude: -75.432, -68.375 degrees

Minimum and maximum for latitude: -54.797, -40.0876 degrees

----- Constants -----

Average distance for isotopic exchange: 540 m

Standard-deviation ratio for data residuals: 28.30 (dimensionless)

----- Constraints for Best-Fit Solution -----

Wind speed: 0.1, 25 m/s

Wind azimuth: 35, 145 degrees

Sea-level temperature: 265, 295 K

Mountain-height number: 0, 1.2 (dimensionless)

Horizontal eddy diffusivity: 0, 1e+06 m^2/s

Average condensation time: 0, 2500 s

d2H for base precipitation: -110.8, -10.4 per mil

d2H latitude gradient for base precipitation: -16.7, 16.7 per mil/deg lat

Residual precipitation after evaporation: 0, 1 (dimensionless)

----- Evaporation Option -----

Leeside evaporative recycling for precipitation state.

----- Solutions From Restart File -----

Restart file: none

----- Solutions From Restart File -----

Restart file: none

----- Best-Fit Search -----

Starting parallel pool (parpool) using the 'local' profile ...

Connected to the parallel pool (number of workers: 27).

Modified controlled random search, fminCRS3

Number of parameters = 9

Number of free parameters = 9

Factor for size of initial search set, mu0 = 25

Factor for size of main search set, mu = 25

Size of initial search set = 225

Size of main search set = 225

Absolute precision for stopping criterion, epsilon = 0.0001

Workers for parallel calculation = 27

Parallel pool using the 'local' profile is shutting down.

----- Estimates for Best-Fit Solution -----

Wind speed: 11.8 m/s

Azimuth: 109.2 degrees

Sea-level temperature: 281.5 K (8.3 °C)

Mountain-height number: 0.187 (dimensionless)

Horizontal eddy diffusivity: 0 m^2/s

Average residence time for cloud water: 140 s

d2H for base precipitation: -43.6 per mil

d2H latitude gradient for base precipitation: -0.859 per mil/deg lat

Residual precipitation after evaporation: 0.82 (dimensionless)

--- Other Variables Related to Best-Fit Solution ---

Saturated Buoyancy frequency: 0.639 mrad/s

d180 for base precipitation: -6.8 per mil

d180 latitude gradient for base precipitation: -0.104 per mil/deg lat

Average residence time for falling precipitation: 1116 s

Water-vapor density at sea level: 8.55 g/m^3

Scale height for water vapor: 2329 m

Average velocity for falling precipitation: 2.1 m/s

Total density at sea level: 1.26 g/m^3

Scale height for total density: 9499 m

Average lapse-rate ratio, gammaSat/gammaEnv: 0.95 (dimensionless)

----- Observed Meteoric Water Line -----

Principal standard deviations: 0.36, 24.54 per mil

Intercept and slope: 12.5 per mil, 8.23

----- Predicted Meteoric Water Line -----

Principal standard deviations: 0.09, 20.95 per mil

Intercept and slope: 14.4 per mil, 8.39

----- Quality of Fit -----

Reduced chi-square: 2.0291

Degrees of freedom: 290

Number of primary samples in wet locations: 299

Number of primary samples: 305

Best-fit parameters:

11.7898 109.223 281.488 0.187347 0.199132 140.178 -0.0435525 -0.000858647
0.821217

Finish time: 19-Aug-2021 02:44:45

Time for current run: 5.33 hours

Program: opiPairPlots
 Start time: 21-Sep-2022 09:50:30
 Path for solutions file:
 /Users/markbrandon/Dropbox (Yale University)/OPI Patagonia/Runs_NP-SP/run024_NP-SP
 Leeside evap, nEvap = 1, more samples BEST SOLUTION/
 Filename for solutions file:
 opiFit_Solutions.txt
 Solutions title:
 run 024, north & south Patagonia, opi 3.6 with lee-side evaporation, free kappa, and new samples

opiPairPlots

Table 1. The parameter constraints used in the search.

Axis Labels	Power-of-10		
	Factors	(Search	Constraints)
1 : U (m/s)	+0	(0.1 , 25)
2 : azimuth	+0	(35 , 145)
3 : T_0 (K)	+0	(265 , 295)
4 : M	+0	(0 , 1.2)
5 : \kappa (m^2/s)	+0	(0 , 1e+06)
6 : \tau_c (s)	+0	(0 , 2500)
7 : \delta^2_0 (%)	-3	(-0.1108 , -0.0104)
8 : d\delta^2_0/d\phi (%/°)	-3	(-0.0167 , 0.0167)
9 : f_P	+0	(0 , 1)

Table 2. The best-fit solution and associated univariate 95-percent confidence limits.

Axis Labels	Estimate	(95% Confidence Limit)	
1 : U (m/s)	11.7899	(11.5143 , 12.1653)
2 : azimuth	109.223	(108.468 , 109.762)
3 : T_0 (K)	281.488	(281.376 , 281.777)
4 : M	0.187323	(0.164133 , 0.206864)
5 : \kappa (m^2/s)	0.186902	(0.0150616 , 237.53)
6 : \tau_c (s)	140.167	(114.208 , 178.201)
7 : \delta^2_0 (%)	-0.0435491	(-0.0446952 , -0.0429646)
8 : d\delta^2_0/d\phi (%/°)	-0.000857804	(-0.00108724 , -0.000629508)
9 : f_P	0.821361	(0.792597 , 0.865856)

----- Background Details about the Search -----

Number of observations for fit: 305

Number of parameters: 9

Number of free parameters: 9

Reduced chi-square for best-fit solution: 2.03014

Degrees of freedom for best-fit solution: 290

Size of solution set: 225

Specified epsilon for stopping criterion, epsilon: 0.0001

Total number of solutions (ignoring nan solutions): 16641

Number of solutions with chiR2==nan: 0

Reduced chi-square for bivariate 95% confidence limit: 2.0508

Number of solutions within bivariate 95% confidence limits: 5828

opiPairPlots, Figure Captions

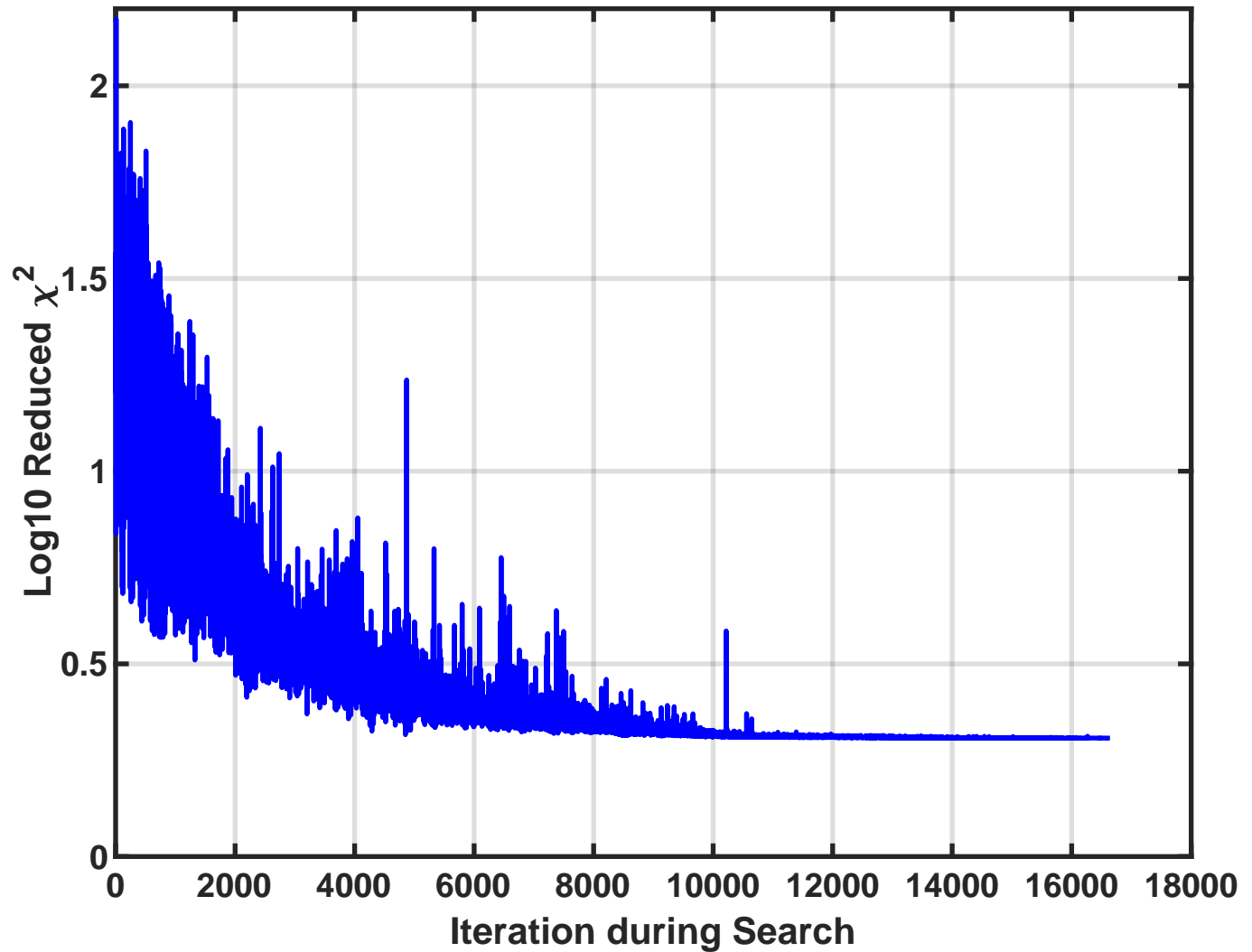
Figure 1. Minimum value of reduced chi-square, χ_r^2 , as a function of the search iteration. The plot shows the evolution and convergence of the search for a best-fit solution.

Figure 2. Termination variable ε as a function of the search iteration. The variable ε is calculated at each step of the search, and is defined by the standard deviation for a set of candidate solutions with the smallest χ_r^2 values. The search is terminated when epsilon is less than a user-specified stopping value, epsilon0 (red line). The solution with the smallest χ_r^2 value at termination is defined as the best-fit solution.

Figure 3. Pair plots showing solutions with χ_r^2 values that lie within the bivariate 95-percent confidence region for each pair of parameters. The selected solutions are projected from the full parameter space into the two-parameter view provided by each plot. The solutions are plotted in order of decreasing χ_r^2 , so that the smallest χ_r^2 solutions are most apparent in the plot. The confidence regions are estimated using the chi2-contour method of Press et al. (2007, p. 812-816).

Figure 4. Pair plot showing χ_r^2 maps for large regions around the best-fit solution, using the same projection and plotting method as described for Figure 3. These plots are helpful for assessing covariance between the parameter estimates, and for judging the convergence of the search and the uniqueness of the best-fit solution.

Fig. 1. Minimum reduced chi-square as function of the search iteration
run 024, north & south Patagonia, opi 3.6 with lee-side evaporation, free kappa, and new samples



**Fig. 2. Termination variable, epsilon, as a function of the search iteration
run 024, north & south Patagonia, op1 3.6 with lee-side evaporation, free kappa, and new samples**

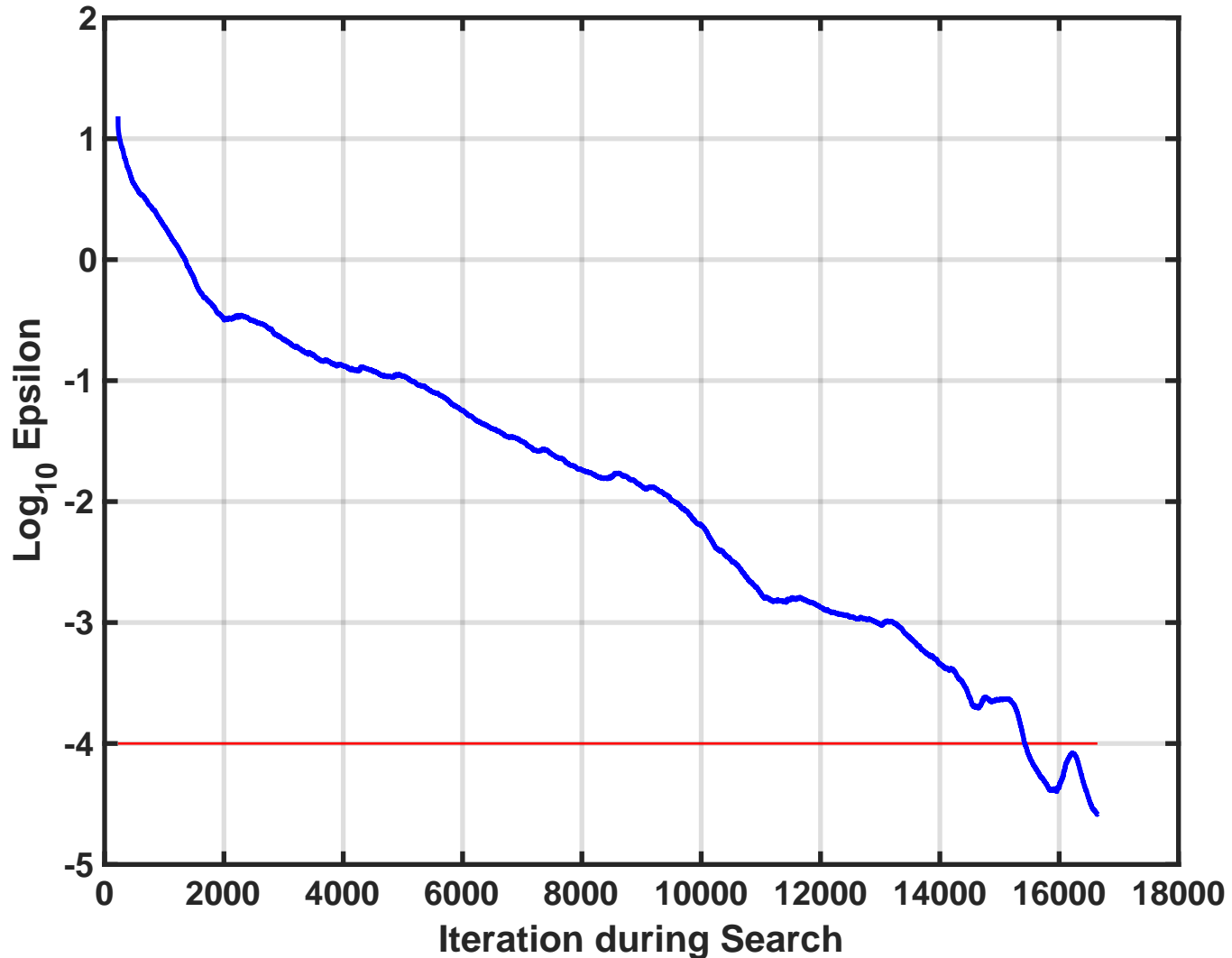


Figure 3. Confidence limits (95%) for best-fit solution.

run 024, north & south Patagonia, op1 3.6 with lee-side evaporation, free kappa, and new samples

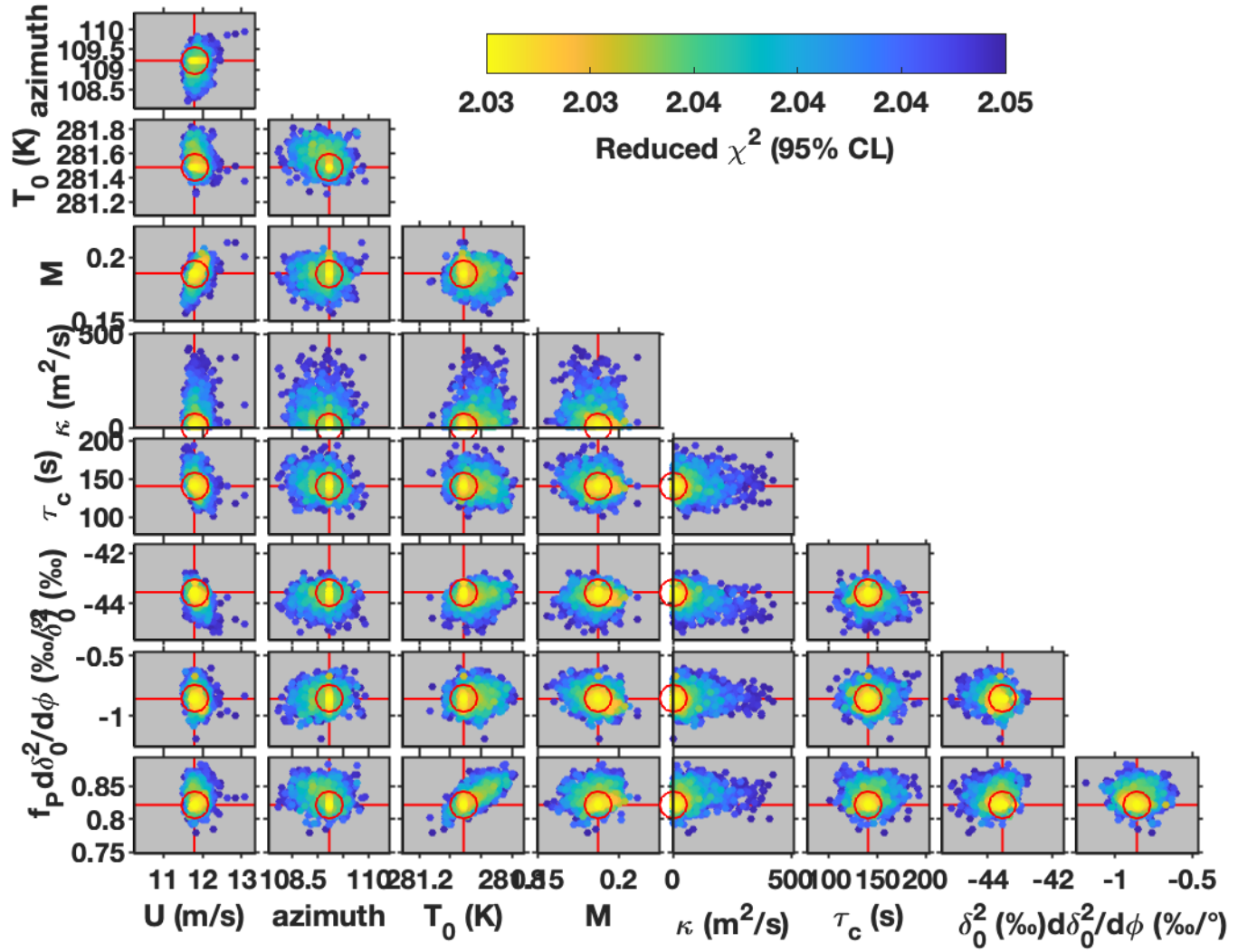
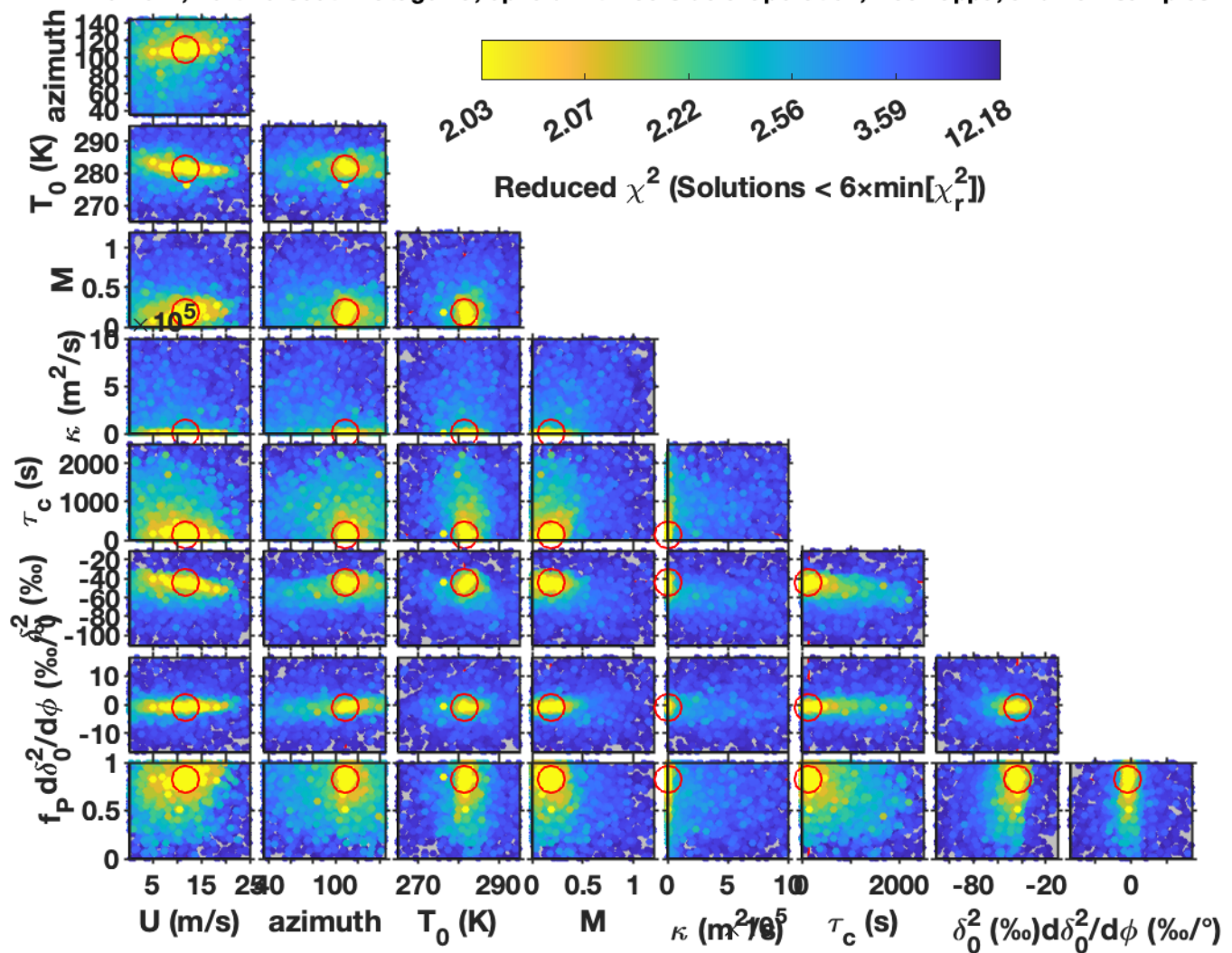


Figure 4. Maps showing reduced χ^2 around best-fit solution.

run 024, north & south Patagonia, op1 3.6 with lee-side evaporation, free kappa, and new samples



Program: opiCalc_OneWind
Start time: 07-Sep-2022 19:23:55

opiCalc_OneWind

Run file path:

/Users/markbrandon/Dropbox (Yale University)/OPI Patagonia/Runs_NP-SP/run024_NP-SP

Leeside evap, nEvap = 1, more samples BEST SOLUTION

Run file name:

run024_NP-SP.run

Run title:

run 024, north & south Patagonia, opi 3.6 with lee-side evaporation, free kappa, and new samples

Path name for data directory:

~/Dropbox/OPI Patagonia/data Patagonia

----- Topography File -----

Topography file: Patagonia topography_Gebco1km.mat

Maximum elevation: 3457 m

Grid size, nx and ny: 1365, 2114

Minimum and maximum for longitude: -80.00000, -62.50000 degrees

Minimum and maximum for latitude: -55.00000, -36.00000 degrees

Grid spacing, dLon and dLat: 0.01283, 0.00899 degrees

Grid spacing, dx and dy: 0.98, 1.00 km

Lon, lat for map origin: -72.66103, -46.76503 degrees

Size of cosine window as fraction of grid size: 0.25 (dimensionless)

Coriolis frequency at map-origin latitude: -0.10625 mrad/s

Lon, lat for section origin: -72.66103, -46.76503 degrees

----- Sample File -----

Sample file: Patagonia Andes North and South Isotopes 29 Jun 2021.xlsx

Number of all samples: 449

Number of primary samples: 305

Number of local primary samples: 1

Number of catchment primary samples: 304

Number of altered samples: 144

Centroid for primary samples, longitude, latitude: -72.66103, -46.76503 degrees

Minimum and maximum for longitude: -75.43200, -68.37500

Minimum and maximum for latitude: -54.79700, -40.08755

----- Constants -----

Characteristic distance for isotopic exchange: 540 m

Standard-deviation ratio for data residuals: 28.30 (dimensionless)

----- Constraints for Best-Fit Solution -----

Wind speed: 0.1, 25 m/s

Wind azimuth: 35, 145 degrees

Sea-level temperature: 265, 295 K (-8.1, 21.9 °C)

Mountain-height number: 0, 1.2 (dimensionless)

Horizontal eddy diffusivity: 0, 1e+06 m^2/s

Average condensation time: 0, 2500 s

d2H for base precipitation: -110.8, -10.4 per mil

d2H latitude gradient for base precipitation: -16.7, 16.7 per mil/deg lat

Residual precipitation after evaporation: 0, 1 (dimensionless)

----- Evaporation Option -----

Evaporative recycling active for precipitation state.

----- Solution -----

Wind speed: 11.8 m/s
Azimuth: 109.2 degrees
Sea-level temperature: 281.5 K (8.3 °C)
Mountain-height number: 0.187 (dimensionless)
Horizontal eddy diffusivity: 0 m^2/s
Average residence time for cloud water: 140 s
 d_{2H} for base precipitation: -43.6 per mil
 d_{2H} latitude gradient for base precipitation: -0.859 per mil/deg lat
Residual precipitation after evaporation: 0.82 (fraction)

---- Other Variables Related to Best-Fit Solution ---

Moist buoyancy frequency: 0.639 mrad/s
 d_{180} for base precipitation: -6.8 per mil
 d_{180} latitude gradient for base precipitation: -0.104 per mil/deg lat
Average residence time for falling precipitation: 1116 s
Water-vapor density at sea level: 8.55 g/m^3
Scale height for water vapor: 2329 m
Average velocity for falling precipitation: 2.1 m/s
Total density at sea level: 1.26 g/m^3
Scale height for total density: 9499 m
Average lapse-rate ratio, gammaSat/gammaEnv: 0.95 (dimensionless)

----- Observed Meteoric Water Line -----

Principal standard deviations: 0.36, 24.54 per mil
Intercept and slope: 12.5 per mil, 8.23

----- Predicted Meteoric Water Line -----

Principal standard deviations: 0.09, 20.95 per mil
Intercept and slope: 14.4 per mil, 8.39

----- Quality of Fit -----

Reduced chi-square: 2.0291
Degrees of freedom: 290
Number of primary samples in wet locations: 299
Number of primary samples: 305
Standard deviation of wet residuals for d_{2H} : 10.4 per mil
Standard deviation of wet residuals for d_{180} : 1.3 per mil
Approximate standard error for predicted d_{2H} : 0.6 per mil
Approximate standard error for predicted d_{180} : 0.1 per mil

----- Computation Time -----

Compute time: 0.75 minutes

----- Mat File -----

Results saved in the run directory as mat file:
/Users/markbrandon/Dropbox (Yale University)/OPI Patagonia/Runs_NP-SP/run024_NP-SP
Leeside evap, nEvap = 1, more samples BEST SOLUTION/opiCalc_OneWind_Results.mat

Program: opiPlots_OneWind
Start time: 07-Sep-2022 19:25:06

opiPlots_OneWind

Run file path:

/Users/markbrandon/Dropbox (Yale University)/OPI Patagonia/Runs_NP-SP/run024_NP-SP

Leeside evap, nEvap = 1, more samples BEST SOLUTION

Run file name:

run024_NP-SP.run

Run title:

run 024, north & south Patagonia, opi 3.6 with lee-side evaporation, free kappa, and new samples

Path name for data directory:

~/Dropbox/OPI Patagonia/data Patagonia

----- Topography File -----

Topography file: Patagonia topography_Gebco1km.mat

Maximum elevation: 3457 m

Grid size, nx and ny: 1365, 2114

Minimum and maximum for longitude: -80.00000, -62.50000 degrees

Minimum and maximum for latitude: -55.00000, -36.00000 degrees

Grid spacing, dLon and dLat: 0.01283, 0.00899 degrees

Grid spacing, dx and dy: 0.98, 1.00 km

Lon, lat for map origin: -72.66103, -46.76503 degrees

Map origin is set to sample centroid.

Size of cosine window as fraction of grid size: 0.25 (dimensionless)

Coriolis frequency at map-origin latitude: -0.10625 mrad/s

Lon, lat for section origin: -72.66103, -46.76503 degrees

----- Sample File -----

Sample file: Patagonia Andes North and South Isotopes 29 Jun 2021.xlsx

Number of all samples: 449

Number of altered samples: 144

Number of primary samples: 305

Number of local primary samples: 1

Number of catchment primary samples: 304

Centroid for primary samples, longitude, latitude: -72.66103, -46.76503 degrees

Minimum and maximum for longitude: -75.43200, -68.37500 degrees

Minimum and maximum for latitude: -54.79700, -40.08755 degrees

----- Constants -----

Characteristic distance for isotopic exchange: 540 m

Standard-deviation ratio for data residuals: 28.30 (dimensionless)

----- Evaporation Option -----

Evaporative recycling active for precipitation state.

----- Solution -----

Wind speed: 11.8 m/s

Azimuth: 109.2 degrees

Sea-level surface-air temperature: 281.5 K (8.3 °C)

Mountain-height number: 0.187 (dimensionless)

Horizontal eddy diffusivity: 0 m^2/s

Average residence time for cloud water: 140 s

d2H for base precipitation: -43.6 per mil

d2H latitude gradient for base precipitation: -0.859 per mil/deg lat

Residual precipitation after evaporation: 0.82 (dimensionless)

---- Other Variables Related to Best-Fit Solution ----
Moist buoyancy frequency: 0.639 mrad/s
d180 for base precipitation: -6.8 per mil
d180 latitude gradient for base precipitation: -0.104 per mil/deg lat
Average residence time for falling precipitation: 1116 s
Water-vapor density at sea level: 8.55 g/m^3
Scale height for water vapor: 2329 m
Average velocity for falling precipitation: 2.1 m/s
Total density at sea level: 1.26 g/m^3
Scale height for total density: 9499 m
Average lapse-rate ratio, gammaSat/gammaEnv: 0.95 (dimensionless)

----- Observed Meteoric Water Line -----

Principal standard deviations: 0.36, 24.54 per mil
Intercept and slope: 12.5 per mil, 8.23

----- Predicted Meteoric Water Line -----

Principal standard deviations: 0.09, 20.95 per mil
Intercept and slope: 14.4 per mil, 8.39

----- Estimates for Lifting Lines-----

The precipitation isotopes are represented using their predicted values from the best-fit OPI solution, either as point estimates if the sample location is designated as "local" (type L), or as the precipitated-weighted value for the upstream catchment if the sample is designated as "catchment" (type C).

The lifting is represented either by local elevation or by the maximum lifting along the upwind path. The elevation and maximum lifting are calculated as either "local" or "catchment" values depending on the designation of the sample (type L or C).

The isotopes are not adjusted for latitudinal gradients (dD2H0_dLat, dD1800_dLat), but this source of error is small and symmetric. The slope of the lines are estimated by least squares and the intercept is held fixed so that it matches the estimated base isotope values (d2H0, d180).

Predicted Isotopes vs Maximum Lifting

Intercept and slope for d2H: -43.6 per mil, -28.9 per mil/km
Intercept and slope for d180: -6.8 per mil, -3.5 per mil/km
[-43.5525 -28.9412 -6.81425 -3.50498]

Predicted Isotopes vs Elevation

Intercept and slope for d2H: -43.6 per mil, -34.5 per mil/km
Intercept and slope for d180: -6.8 per mil, -4.2 per mil/km

----- Quality of Fit -----

Reduced chi-square: 2.0291
Degrees of freedom: 290
Number of wet locations for primary samples: 299
Number of primary samples: 305

----- Computation Time -----

Compute time: 0.18 minutes

opiPlots_OneWind, Figure Caption

Figure 1. Comparison of observed and predicted isotope values (circles) for samples of primary meteoric water. The predicted values are determined by a least-squares fit of the observed isotopic data to a one-wind OPI model. The fit is considered good if the data follow the 1:1 reference (gray line). The red square shows the estimated composition of base precipitation.

Figure 2. Craig plot showing $\delta^2\text{H}$ versus $\delta^{18}\text{O}$ compositions for primary samples. Gray and blue circles show observed and predicted values, respectively. The gray line is the meteoric water line (MWL) as determined by total least squares fit of the observed data. The red point shows the estimated average for the isotopic composition of base precipitation, and the red ellipse shows the estimated standard-deviation variation of that composition. The ellipse shows the covariance of $\delta^2\text{H}$ and $\delta^{18}\text{O}$, which is mainly due to natural stochastic variation (analytical errors are typically much smaller in comparison). The ratio of the principal standard deviations is set to 28.3, as estimated using observed monthly variation for the GNIP station at Coyhaique, Chile. The magnitude and orientation of the principal standard deviations are determined for each run, using the total least-squares method. The best-fit solution uses this result when calculating reduced chi-square (i.e., the residuals for $\delta^2\text{H}$ and $\delta^{18}\text{O}$ for each sample are scaled and combined using the covariance matrix corresponding to the standard-deviation ellipse).

Figure 3. Craig plot showing $\delta^2\text{H}$ versus $\delta^{18}\text{O}$ compositions for primary and altered samples. The blue circles are predicted values for primary samples, and the red circles are observed values for altered samples. The offset of the altered samples from the MWL (gray line) is due to evaporation. The dark green line associated with each altered sample shows the path, as predicted by the OPI solution, from a primary composition on the MWL to the observed altered composition. The average slope of the alteration paths is about five, which is a typical for evaporation of meteoric water (Criss, 1999).

Figure 4. Standardized residuals for best-fit solution. The plots here allow inspection of the standard residuals as a function of horizontal location (easting, northing) in the model domain. A good least-squares fit is characterized by magnitudes that are no greater than about three, and that vary independently across the model domain.

Figure 5. Predicted precipitation isotopes (blue circles) for sample locations as a function of maximum lifting. Maximum lifting is approximated by the maximum elevation of the topography along the path upwind of the sample location. The end point for this path calculation is offset upwind to account for the average horizontal advection of the precipitation as it drops along its fall path. Least-squares is used to estimate the best-fit linear fit to the data, as shown by the gray line, and equation in each plot. Precipitation isotope data typically show a tighter linear relationship with respect to maximum lifting, as opposed to local elevation (see figure 6 for comparison). Note that the calculation of the plotted data accounts for the designation for each sample, whether “local” or “catchment”.

Figure 6. Predicted precipitation isotopes (blue circles) for sample locations as a function of local elevation, which is defined as the land surface elevation below the point where precipitation first separates from cloud water. This calculation accounts for downwind offset of precipitation along its fall path. See Figure 5 for details about the calculation and layout of the figure.

Figure 7. One-dimensional temperature field for the base-state atmosphere. The base temperature field is solved by vertical integration of the equation of state for a moist atmosphere, starting with a specified sea-level surface-air temperature T_0 and an atmosphere with a uniform moist buoyancy frequency N_m . The left plot shows the actual temperature profile, which is called the environmental temperature. The right plot shows the lapse rate (negative vertical temperature gradient) for the environmental temperature profile, and the moist adiabatic lapse rate, which is a reference gradient observed for local vertical displacement of a moist parcel of air. The lapse rates are small near the surface (usually in the range from 4.5 to 6.5 $^{\circ}\text{C}/\text{km}$), and increase to a limiting value of 10 $^{\circ}\text{C}/\text{km}$ in the upper atmosphere. The reason is the exponentially decreasing water vapor with elevation. Note that if the parameter N_m were increased, the difference between the moist and environmental lapse rates would increase and the atmosphere would become more stably stratified and resistant to vertical displacements.

Fig. 1. Observed versus predicted isotope values

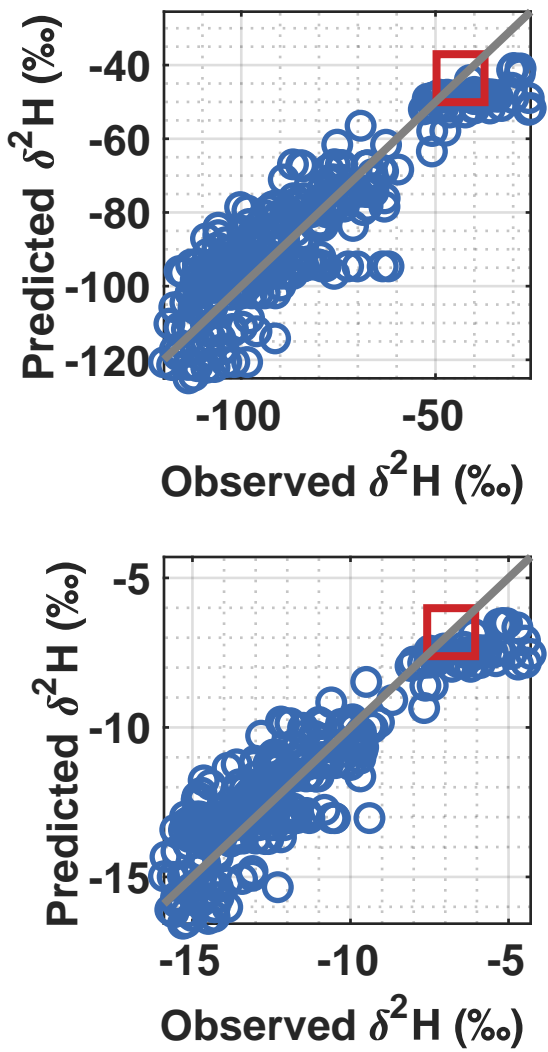


Fig. 2. Craig plot of primary samples

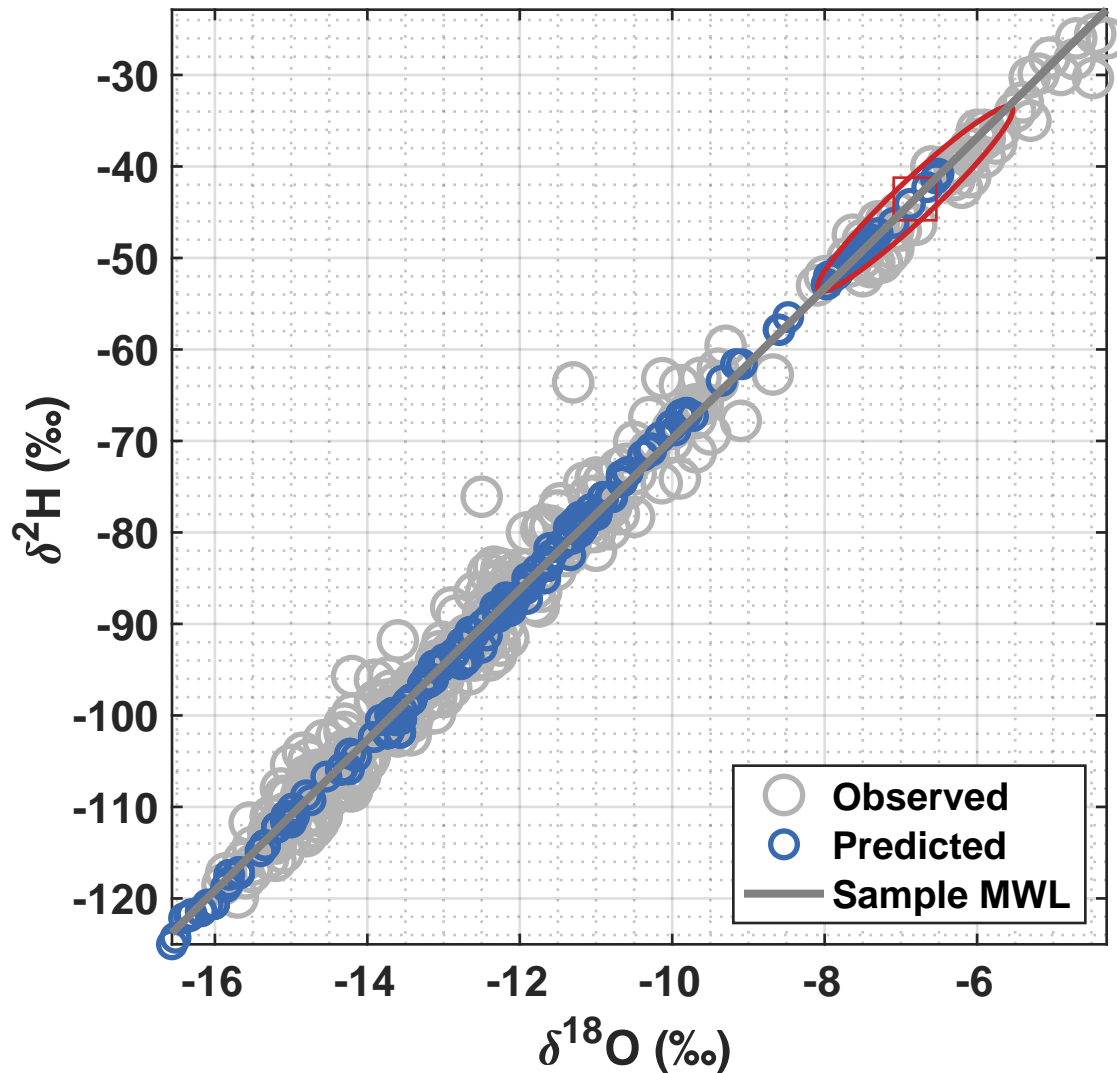


Fig. 3. Craig plot of primary and altered samples

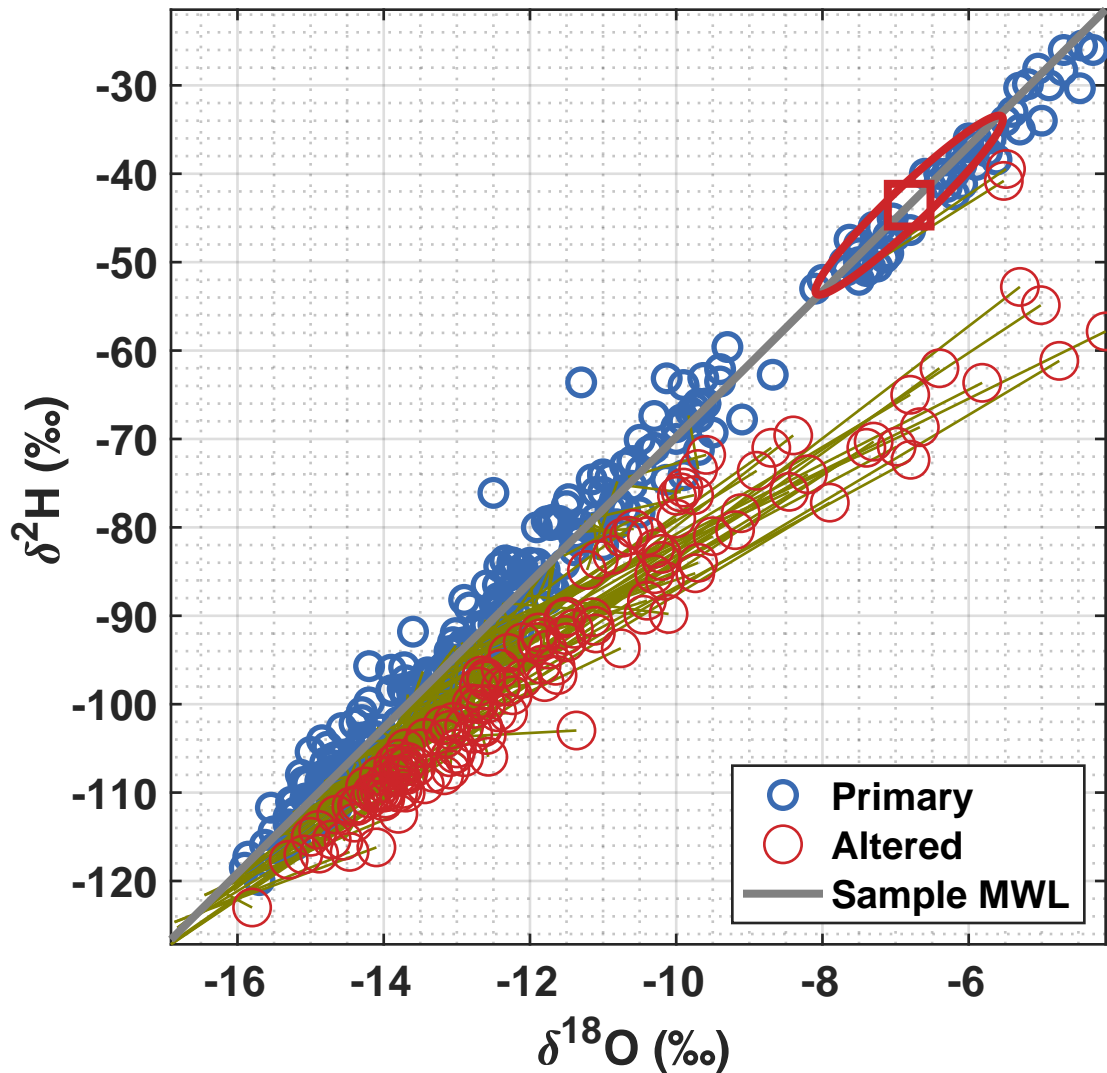


Fig. 4. Standardized residuals for best-fit solution

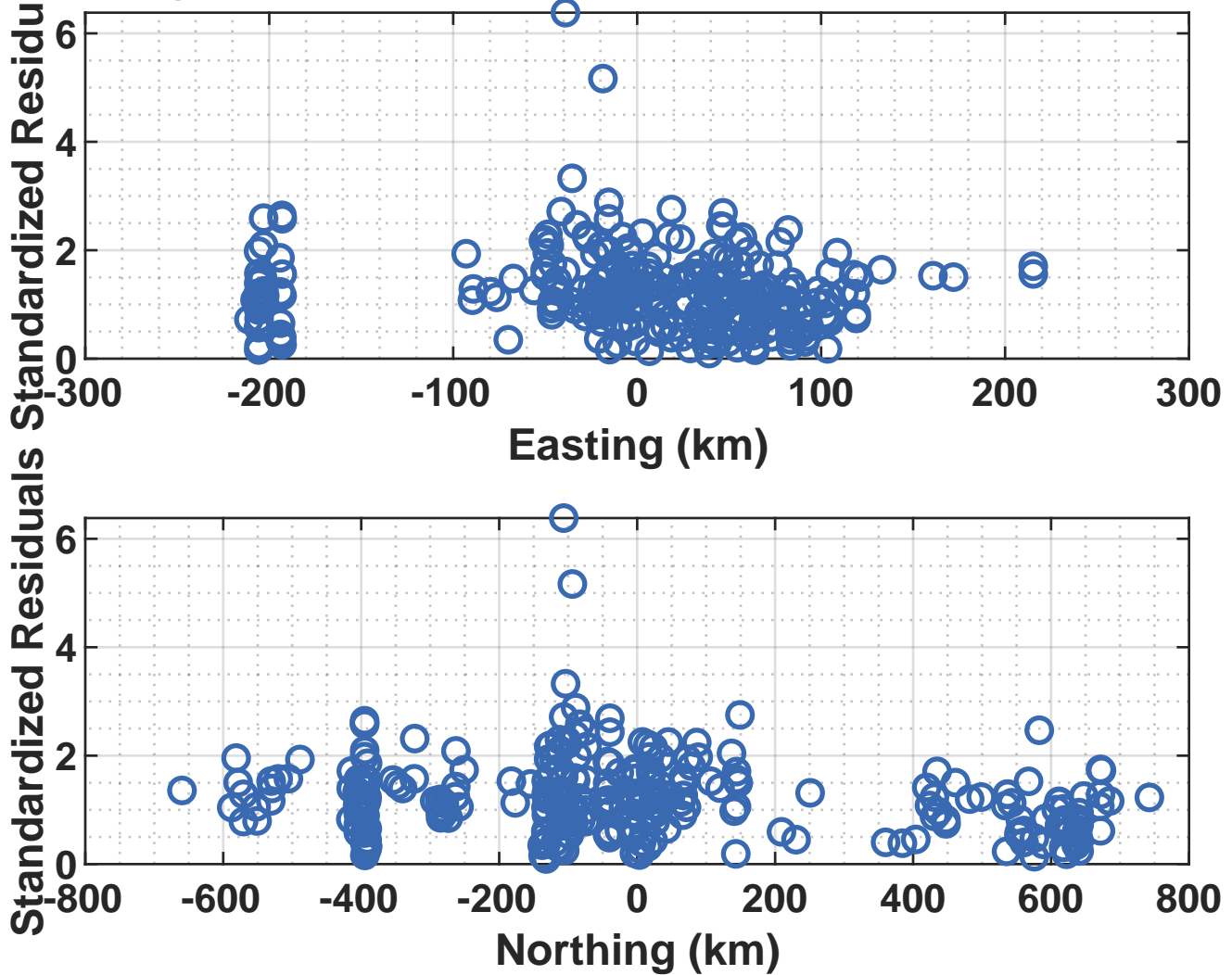


Fig. 5. Predicted isotopes versus maximum lifting

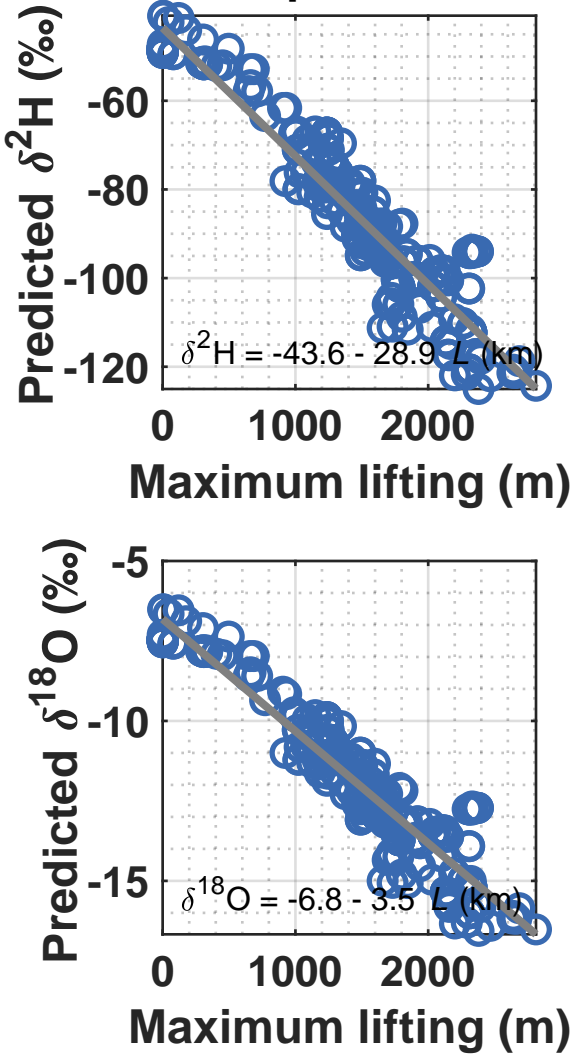


Fig. 6. Predicted isotopes versus elevation

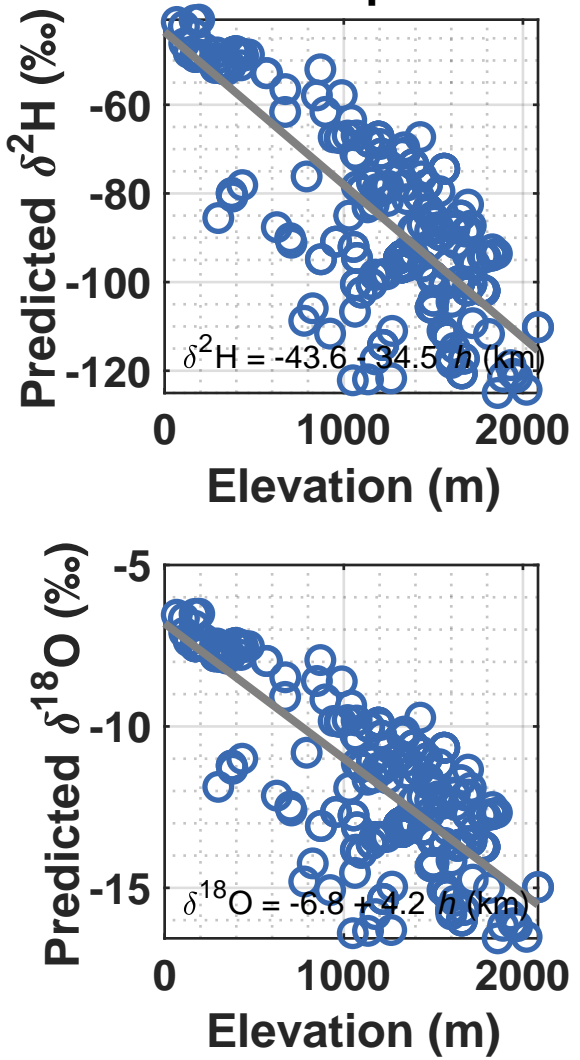
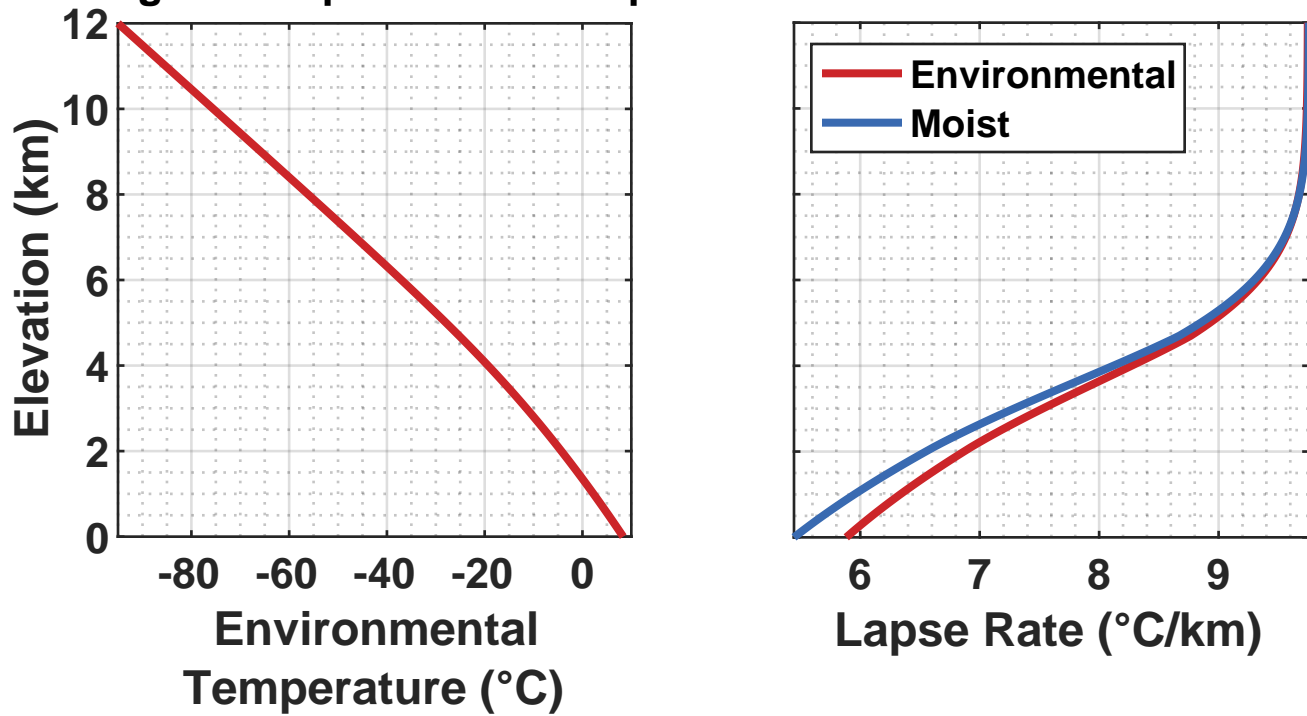


Fig. 7. Temperature and lapse rates versus elevation



Program: opiMaps_OneWind
Start time: 07-Sep-2022 23:40:10

opiMaps_OneWind

Run file path:

/Users/markbrandon/Dropbox (Yale University)/OPI Patagonia/Runs_NP-SP/run024_NP-SP
Leeside evap, nEvap = 1, more samples BEST SOLUTION

Run file name:

run024_NP-SP.run

Run title:

run 024, north & south Patagonia, opi 3.6 with lee-side evaporation, free kappa, and new samples

Path name for data directory:

~/Dropbox/OPI Patagonia/data Patagonia

----- Topography File -----

Topography file: Patagonia topography_Gebco1km.mat

Maximum elevation: 3457 m

Grid size, nx and ny: 1365, 2114

Longitude, minimum and maximum: -80.00000, -62.50000 degrees

Latitude, minimum and maximum: -55.00000, -36.00000 degrees

Grid spacing, dLon and dLat: 0.01283, 0.00899 degrees

Grid spacing, dx and dy: 0.98, 1.00 km

User-defined map limits, longitude: -77.00000, -68.00000 degrees

User-defined map limits, latitude: -54.00000, -39.00000 degrees

Continental-divide file: Patagonia_RidgeLineLonLat.mat

Lon, lat for map origin: -72.66103, -46.76503 degrees

Map origin is set to sample centroid.

Size of cosine window as fraction of grid size: 0.25

Coriolis frequency at map-origin latitude: -0.10625 mrad/s

Lon, lat for section origin: -72.66103, -46.76503 degrees

----- Sample File -----

Sample file: Patagonia Andes North and South Isotopes 29 Jun 2021.xlsx

Number of all samples: 449

Number of altered samples: 144

Number of primary samples: 305

Number of local primary samples: 1

Number of catchment primary samples: 304

Centroid for primary samples, longitude, latitude: -72.66103, -46.76503 degrees

Minimum and maximum for longitude: -75.43200, -68.37500 degrees

Minimum and maximum for latitude: -54.79700, -40.08755 degrees

----- Constants -----

Characteristic distance for isotopic exchange: 540 m

Standard-deviation ratio for data residuals: 28.30 (dimensionless)

----- Evaporation Option -----

Evaporative recycling active for precipitation state.

----- Solution -----

Wind speed: 11.8 m/s

Azimuth: 109.2 degrees

Sea-level surface-air temperature: 281.5 K (8.3 °C)

Mountain-height number: 0.187 (dimensionless)

Horizontal eddy diffusivity: 0 m^2/s

Average residence time for cloud water: 140 s

d2H for base precipitation: -43.6 per mil
d2H latitude gradient for base precipitation: -0.859 per mil/deg lat
Residual precipitation after evaporation: 0.82 (dimensionless)

---- Other Variables Related to Best-Fit Solution ---

Moist buoyancy frequency: 0.639 mrad/s
d180 for base precipitation: -6.8 per mil
d180 latitude gradient for base precipitation: -0.104 per mil/deg lat
Average residence time for falling precipitation: 1116 s
Water-vapor density at sea level: 8.55 g/m³
Scale height for water vapor: 2329 m
Average velocity for falling precipitation: 2.1 m/s
Total density at sea level: 1.26 g/m³
Scale height for total density: 9499 m
Average lapse-rate ratio, gammaSat/gammaEnv: 0.95 (dimensionless)

----- Streamlines, and Cloud Water -----

Vertical exaggeration for streamline figure: 20000 (dimensionless)
Starting elevation for streamlines: 2000 m
Mean height of cloud water relative to land surface: 1590 m

Compute time: 2.65 minutes

opiMaps_OneWind, Figure Caption

Figure 1. Topography and sample locations (black circles). A catchment sample is indicated by a red polygon, which indicates the extent of the upslope catchment. A local sample has no red polygon. The black arrow shows the best-fit wind direction. The black line and square indicate the origin and extent of the cross section (origin defined by the user, orientation is parallel to the best-fit wind direction). The thick gray line marks the drainage divide (if provided by the user).

Figure 2. Observed $\delta^2\text{H}$ composition (colored circles) for samples of primary meteoric water. The color bar on the right indicates the correspondence between symbol color and composition. Other features are the same as for Figure 1.

Figure 3. Observed deuterium-excess, d , for samples of altered meteoric water.

Figure 4. Predicted orographic precipitation rate (mm/h), as indicated by the specified one-wind OPI solution. White regions indicate no precipitation.

Figure 5. Predicted streamlines (red lines) for atmospheric flow, as indicated by the specified one-wind OPI solution. The streamlines start at an elevation of 2000 m at the upwind limit of the model domain.

Figure 6. Cross section of climate state for the specified one-wind OPI solution. Top panel shows topography (brown), air flow (black streamlines), cloud-water distribution (gray), and precipitation fall lines (dotted black lines). The Wegener-Bergeron-Findeisen zone is delimited by the two blue lines, and marks the upward transition in the atmosphere from rain to ice. The center panel shows the predicted orographic precipitation. The bottom panel shows the predicted distribution of $\delta^2\text{H}$ in precipitation. The dashed line shows the $\delta^2\text{H}$ composition of base precipitation, which includes an estimated latitudinal gradient. The section is parallel to the wind direction, and the origin is set at a user-specified location.

Figure 7. Predicted $\delta^2\text{H}$ for orographic precipitation, as indicated by the specified one-wind OPI solution. White regions indicate no precipitation.

Figure 8. Predicted $\delta^{18}\text{O}$ for orographic precipitation, as indicated by the specified one-wind OPI solution. White regions indicate no precipitation.

Figure 9. Surface temperature, as indicated for the specified one-wind OPI solution.

Figure 10. Predicted moisture ratio, as indicated for the specified one-wind OPI solution. The atmosphere starts with a moisture ratio of one at the upwind limit of the model domain.

Figure 11. Location of outlier samples. The blue points show all sample locations. Standardized residuals are reported adjacent to those samples that have large misfits (standardized residuals > 3) relative to the best-fit solution.

Figure 12. Surface velocity ratio, u'/U , for the specified one-wind OPI solution, where U is the mean wind speed, and u' is the perturbation in wind speed relative to the mean for a location

at the topographic surface. This map is useful for assessing if the solution is consistent with the linear approximation used to calculate the wind velocity field, and if there are areas with significant blocking. The linear approximation requires that $|u'/U| < 1$, and blocking is indicated when $u'/U > 1$.

Fig. 1. Topography and sample locations

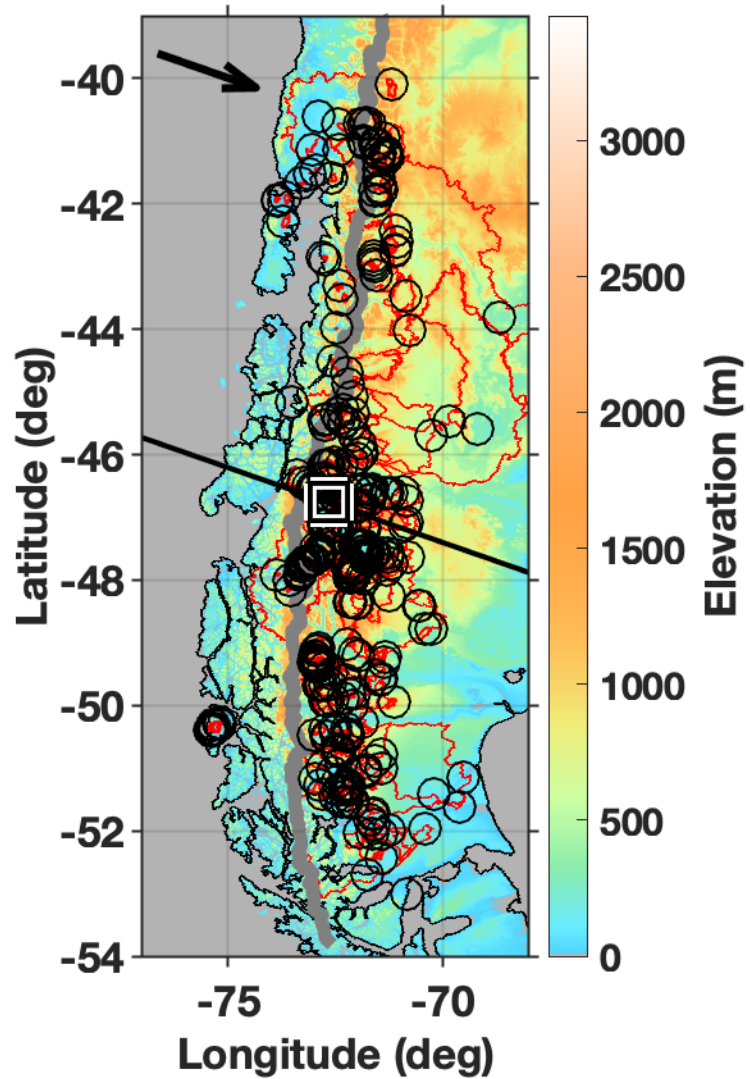


Fig. 2. Observed $\delta^2\text{H}$ for primary samples

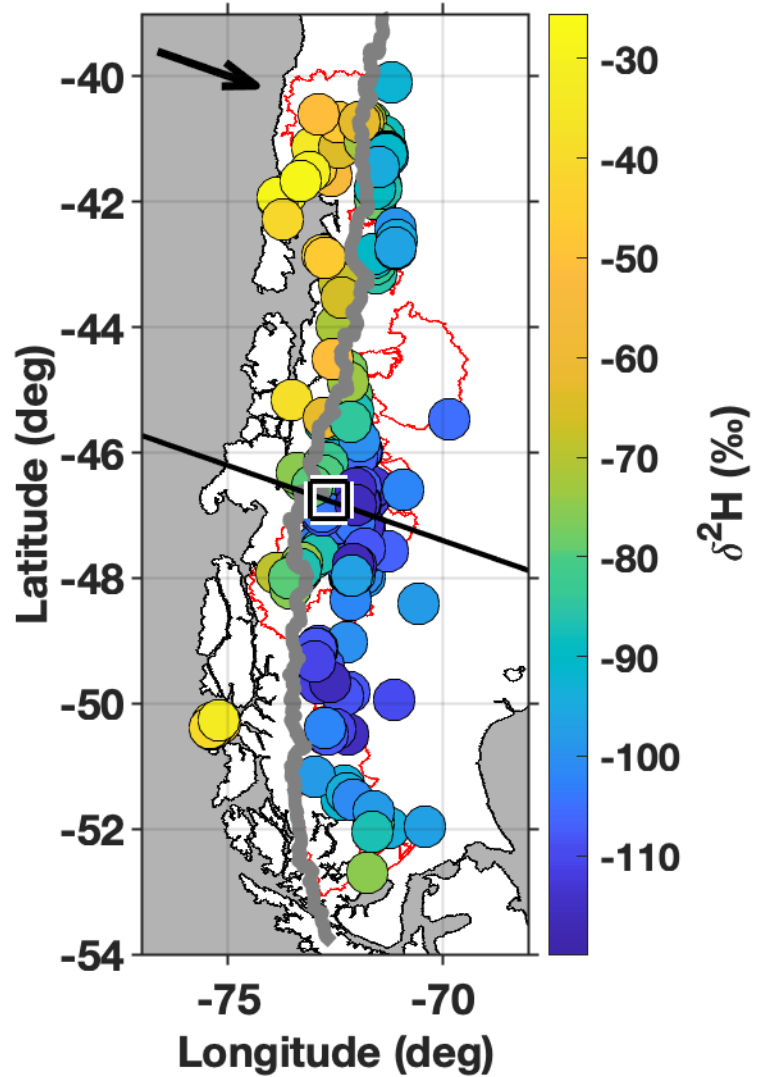


Fig. 3. Deutrium-excess for altered samples

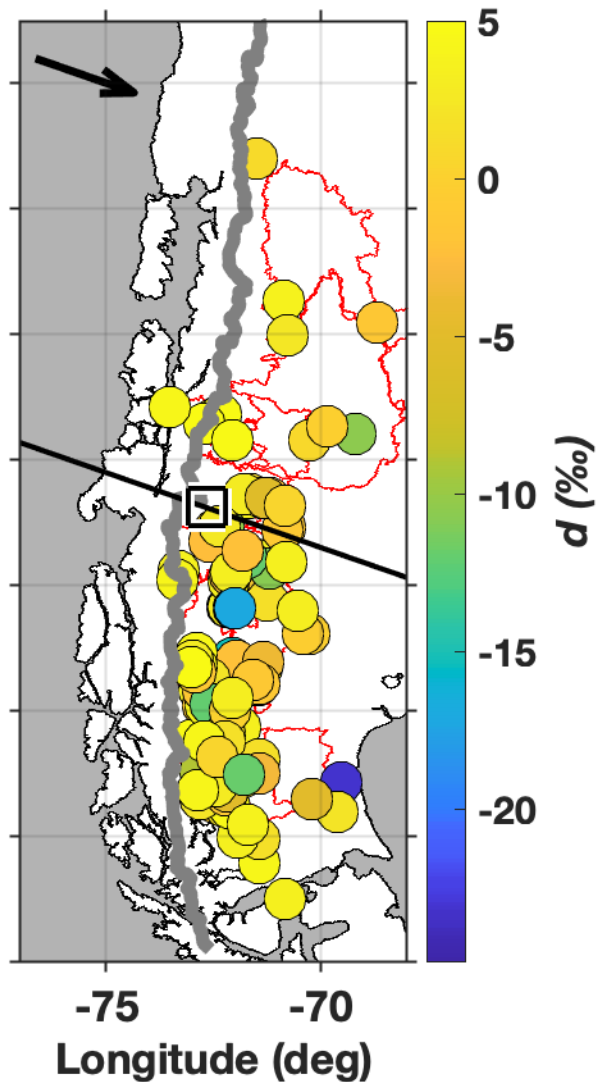


Fig. 4. Precipitation rate

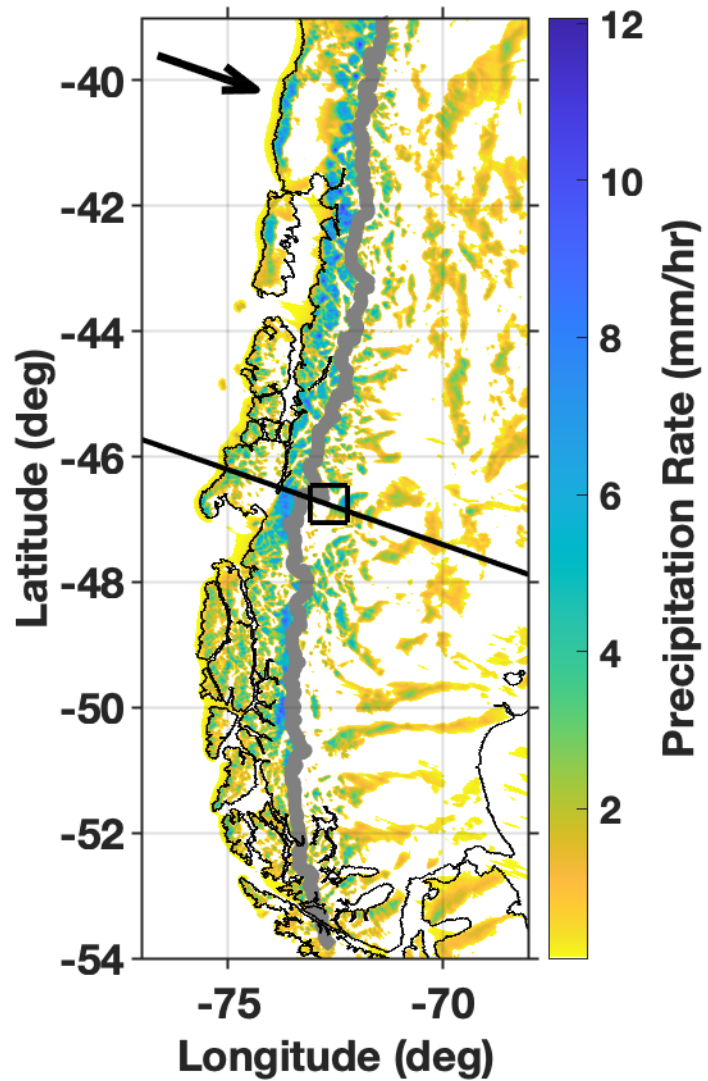


Fig. 5. Moisture ratio

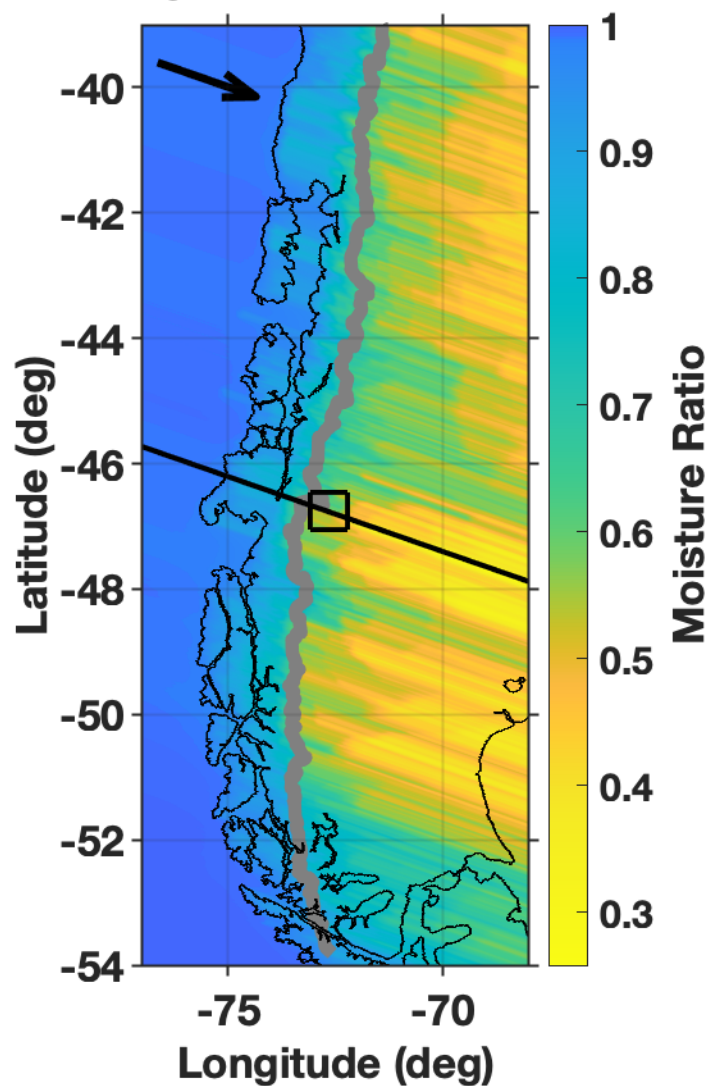


Fig. 6. Surface relative humidity

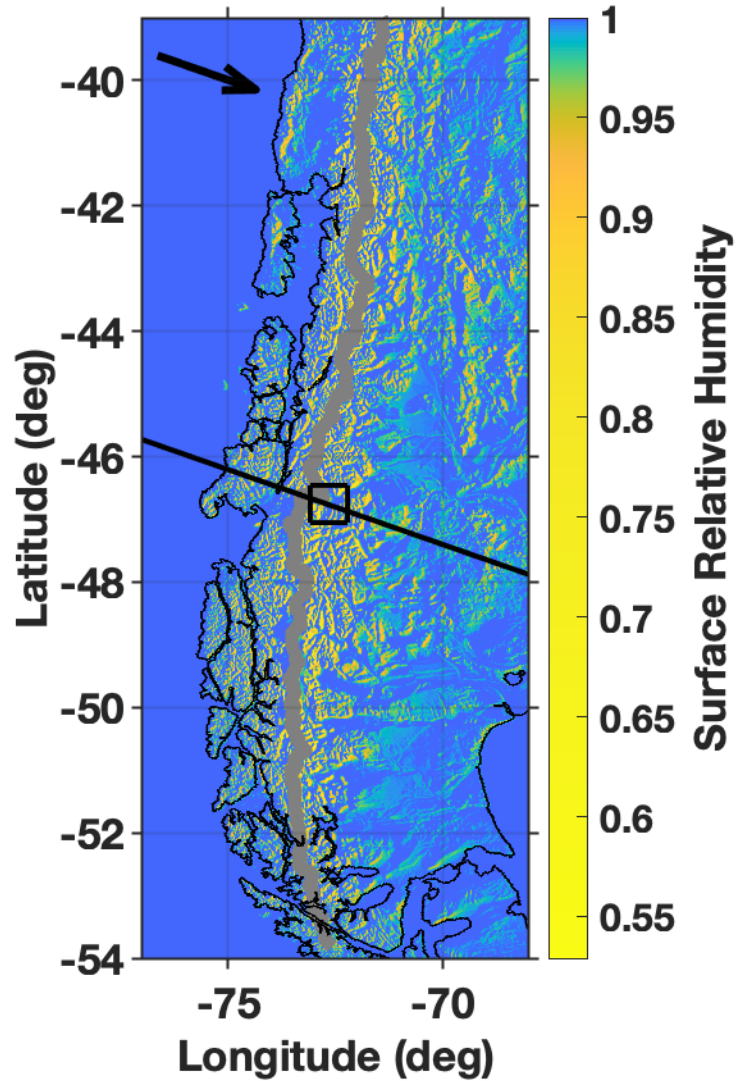


Fig. 7. Streamlines starting at 2000 m elevation

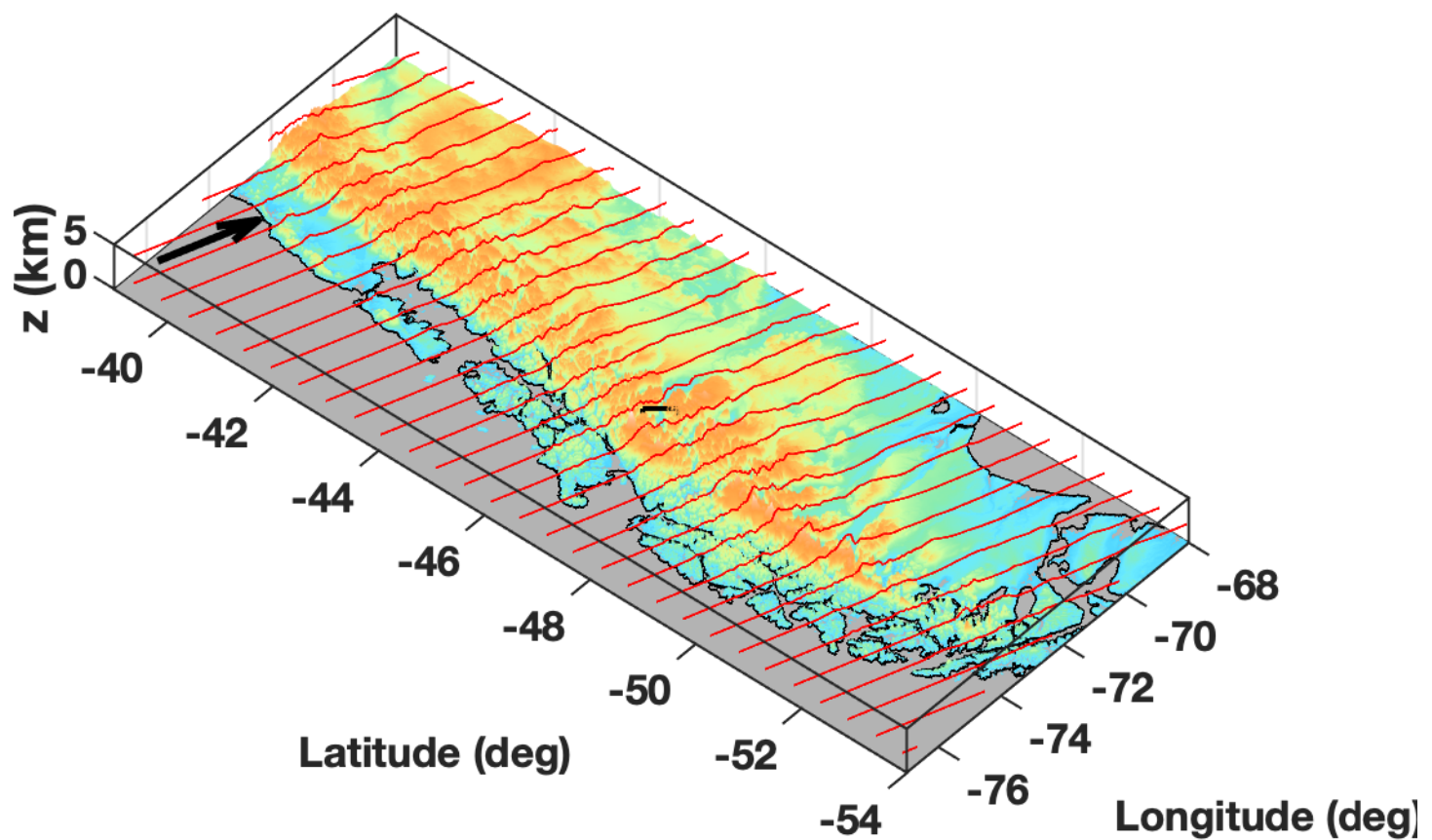


Fig. 8. Cross section

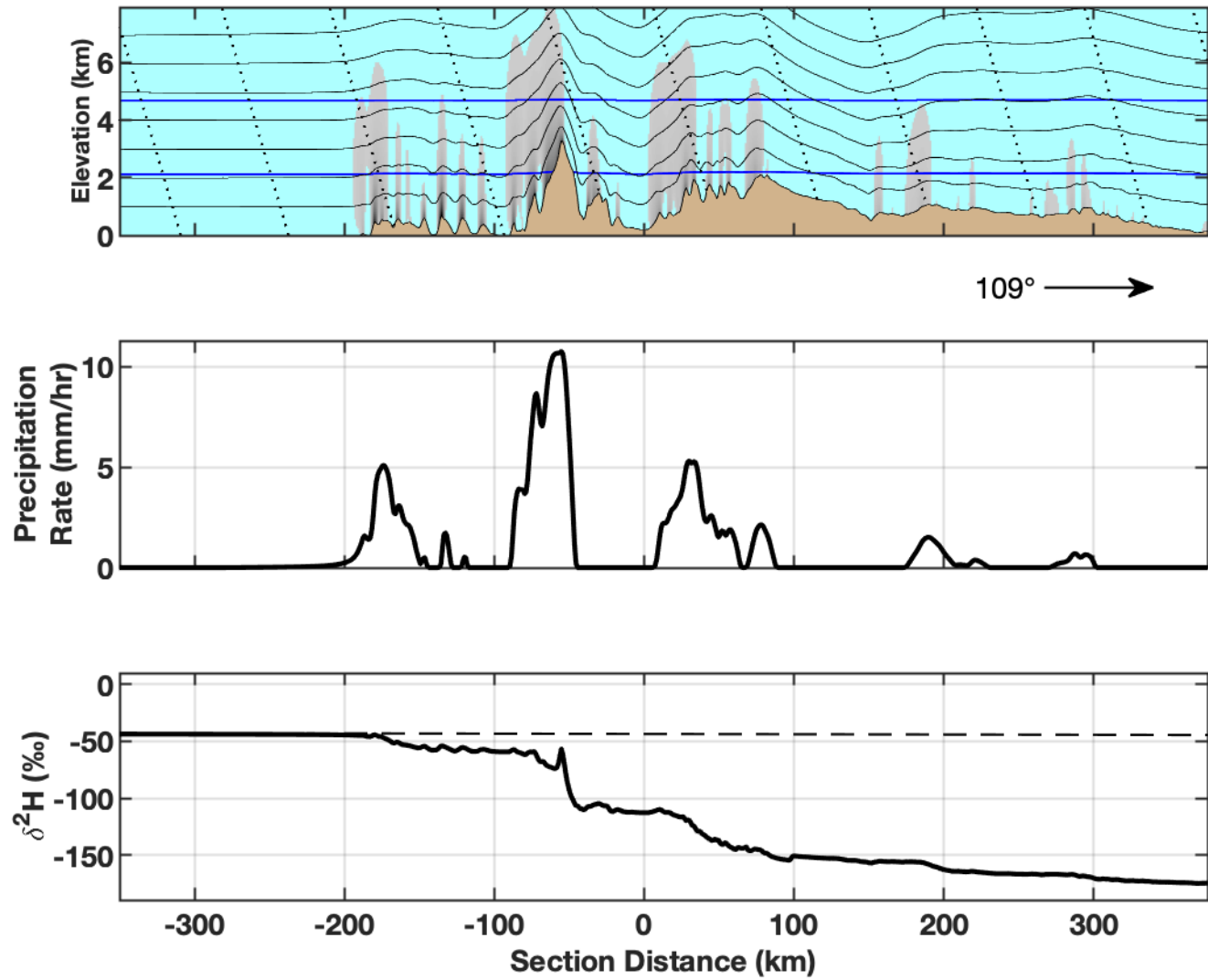


Fig. 9. Predicted precipitation $\delta^2\text{H}$

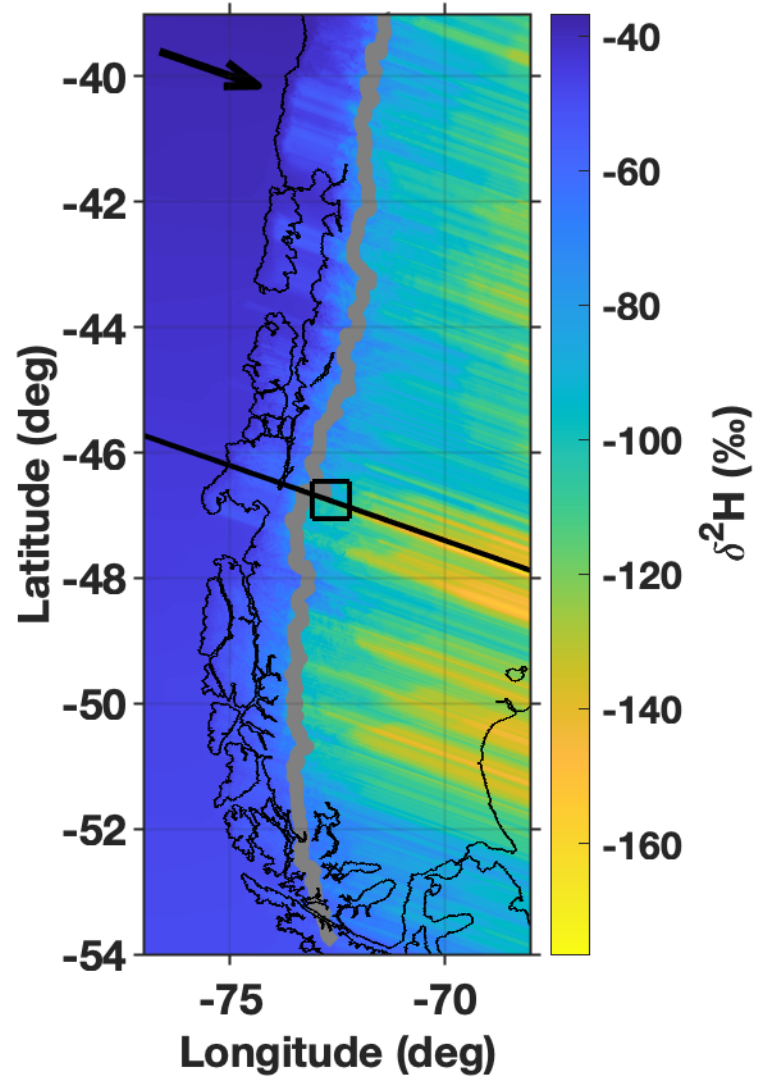


Fig. 10. Predicted precipitation $\delta^{18}\text{O}$

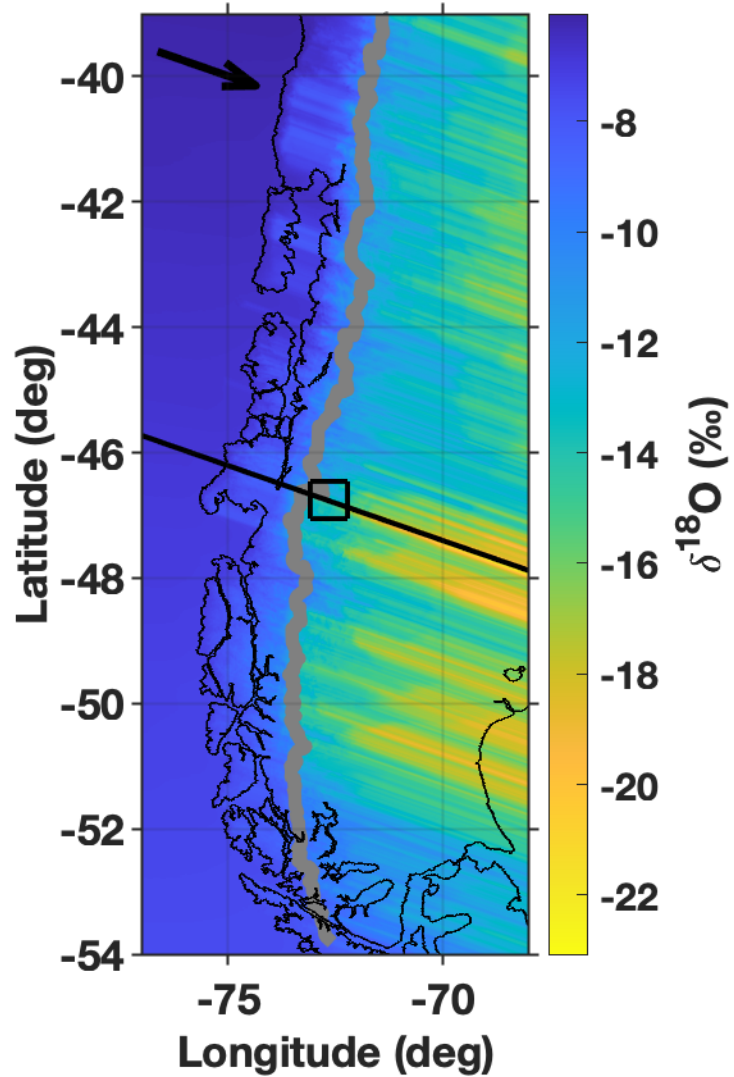


Fig. 11. Surface-air temperature

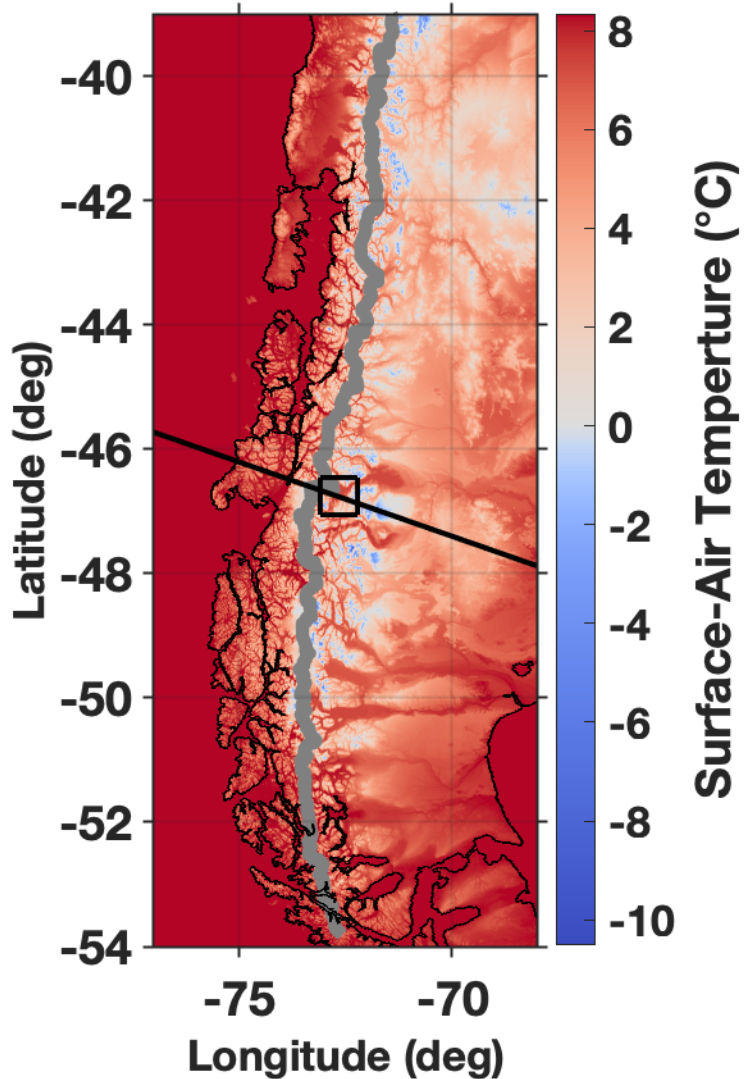


Fig. 12. Surface velocity ratio, u'/U

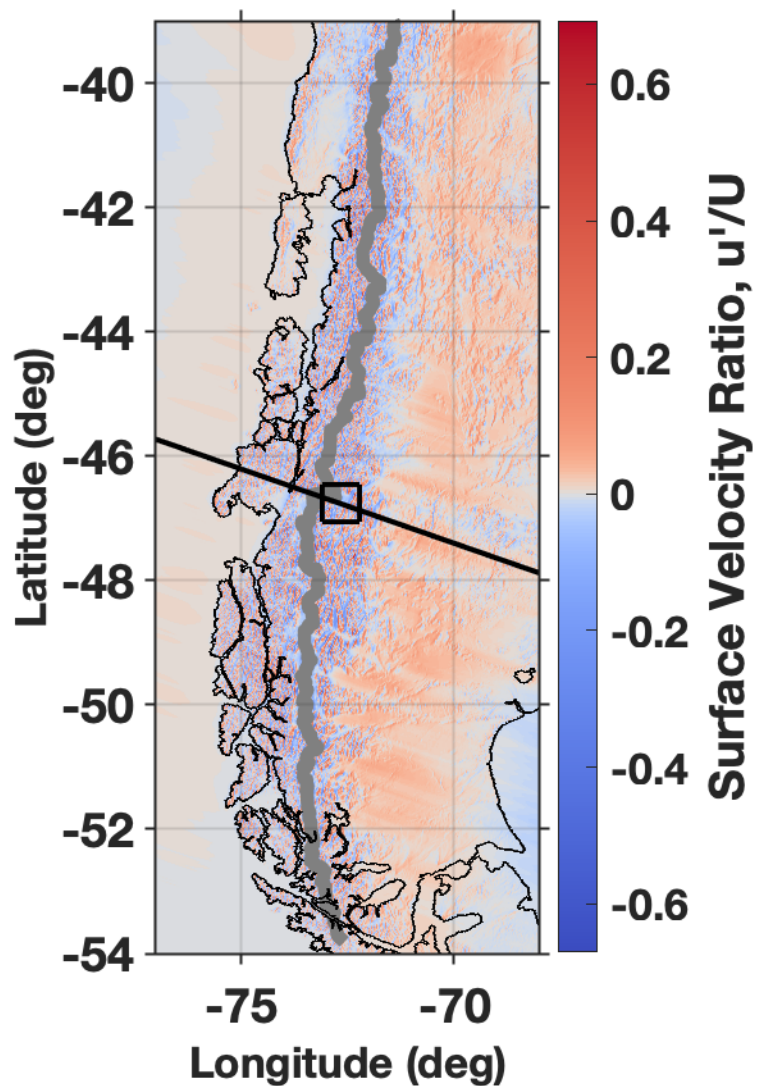


Figure 13. Location of outliers

